Article

Spatially resolved mapping of cells associated with human complex traits

https://doi.org/10.1038/s41586-025-08757-x

Received: 12 May 2024

Accepted: 7 February 2025

Published online: 19 March 2025

Open access

Check for updates

Liyang Song[1,2,3], Wenhao Chen[1,2,3], Junren Hou[1,2], Minmin Guo[1,2] & Jian Yang[1,2]✉

Depicting spatial distributions of disease-relevant cells is crucial for understanding disease pathology[1,2]. Here we present genetically informed spatial mapping of cells for complex traits (gsMap), a method that integrates spatial transcriptomics data with summary statistics from genome-wide association studies to map cells to human complex traits, including diseases, in a spatially resolved manner. Using embryonic spatial transcriptomics datasets covering 25 organs, we benchmarked gsMap through simulation and by corroborating known trait-associated cells or regions in various organs. Applying gsMap to brain spatial transcriptomics data, we reveal that the spatial distribution of glutamatergic neurons associated with schizophrenia more closely resembles that for cognitive traits than that for mood traits such as depression. The schizophrenia-associated glutamatergic neurons were distributed near the dorsal hippocampus, with upregulated expression of calcium signalling and regulation genes, whereas depression-associated glutamatergic neurons were distributed near the deep medial prefrontal cortex, with upregulated expression of neuroplasticity and psychiatric drug target genes. Our study provides a method for spatially resolved mapping of trait-associated cells and demonstrates the gain of biological insights (such as the spatial distribution of trait-relevant cells and related signature genes) through these maps.

The composition and spatial organization of cells within a tissue are critical to its function and can also serve as indicators of its health status[1]. The advancement in spatial transcriptomics (ST), which enables the profiling of gene expression levels of cells in their native spatial positions, represents a promising avenue for investigating cell spatial organizations and uncovering related biological mechanisms[3,4]. In recent years, an increasing number of studies have utilized ST technologies to explore cell spatial organization in diverse tissues[5–7]. However, a substantial knowledge gap persists in identifying cells that are most relevant to complex traits or diseases and mapping their spatial distribution within a tissue.

To identify trait-associated cells or cell types, previous studies have proposed genetics-informed strategies that integrate data from genome-wide association studies (GWAS) of complex traits, including diseases, with single-cell RNA-sequencing (scRNA-seq) data[8–11]. Although these methods can pinpoint trait-associated cells, they encounter challenges in mapping the spatial distribution of these identified cells owing to the lack of cell spatial positional information in scRNA-seq data. These scRNA-seq-based methods can, in principle, be applied to ST data. However, owing to the absence of modelling for cell spatial coordinates and the high level of technical noise in ST data[12], they have limited power in spatially aware mapping of trait-associated cells. Although previous studies[13] have associated spatial domains with complex traits, these analyses are not at single-cell resolution, limiting their ability to profile the spatial distribution of trait-associated cells. Consequently, there is a need for new methods that can integrate ST data into GWAS for fine-scale spatially resolved mapping of trait-associated cells.

In this study, we introduce gsMap, a method that integrates high-resolution ST data and GWAS summary statistics for spatially resolved mapping of trait-associated cells. Utilizing embryonic ST datasets covering 25 organs, we assessed the specificity of gsMap through simulated GWAS data and the sensitivity of the method by recapitulating known associations between cells in different organs and a range of complex traits. Applying gsMap to brain ST datasets, we generated extensive trait–brain cell association maps encompassing 30 human brain-related complex traits.

Overview of gsMap

The fundamental concept of gsMap involves assessing whether genetic variants, predominantly single nucleotide polymorphisms (SNPs), located in or near genes highly expressed in a spot in ST data are enriched for genetic associations with a trait of interest (Methods and Supplementary Note, sections 1–3). Each ST section is required to include transcriptome-wide gene expression profiles and spatial coordinates of individual spots. Here, a 'spot' refers to a cell in high-resolution ST platforms (for example, Stereo-seq cell-bin mode) or a cluster of cells in conventional ST platforms (such as 10X Visium). gsMap consists of three steps. First, gsMap leverages spot homogeneity to address sparsity and technical noise in ST data. gsMap uses a graph neural network (GNN) to identify homogeneous spots for each focal spot in terms of

[1]School of Life Sciences, Westlake University, Hangzhou, China. [2]Westlake Laboratory of Life Sciences and Biomedicine, Hangzhou, China. [3]These authors contributed equally: Liyang Song, Wenhao Chen. ✉e-mail: jian.yang@westlake.edu.cn

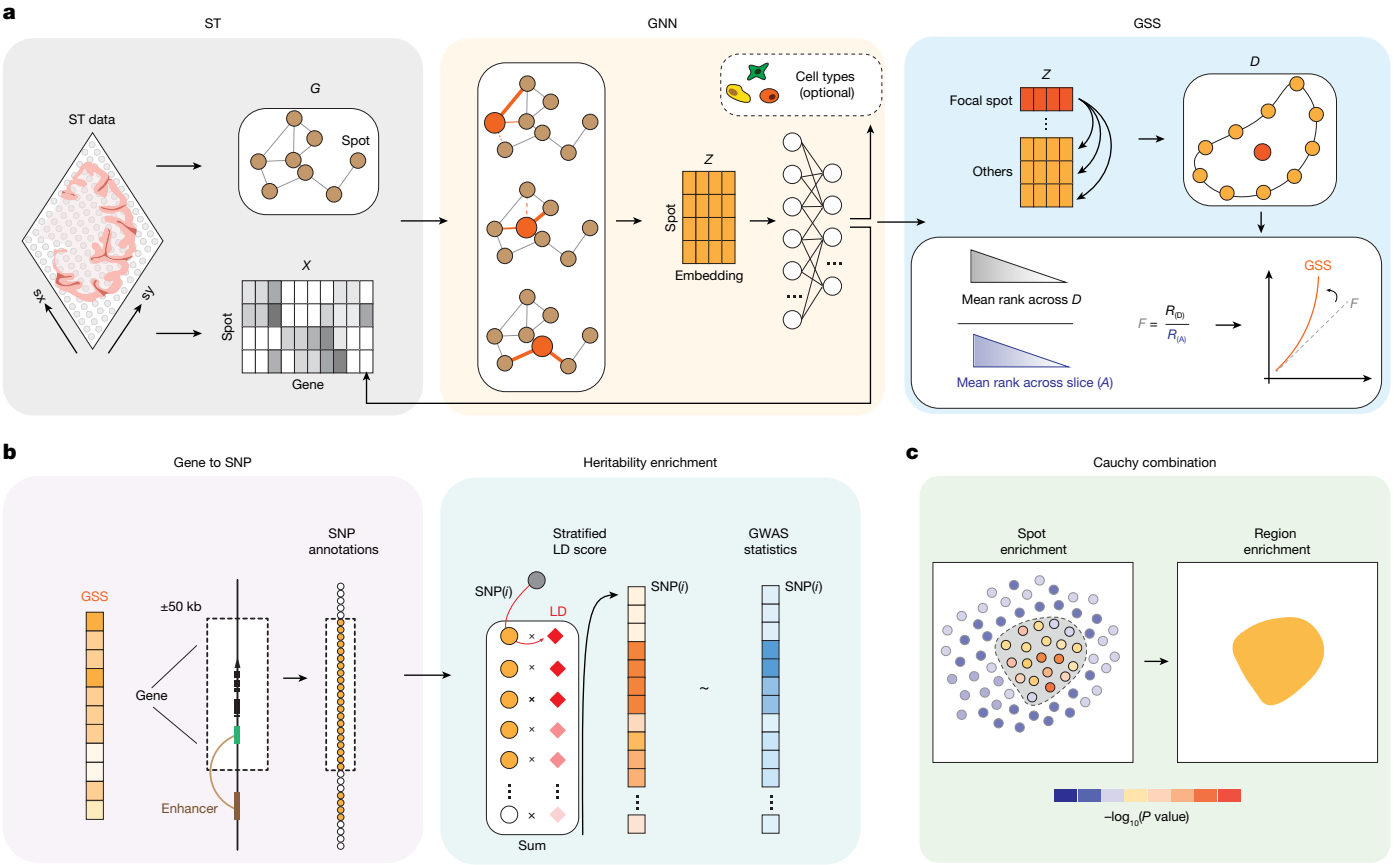

Fig. 1 | Schematics of the gsMap method. a, gsMap begins by using a GNN to learn embeddings that integrate gene expression levels, spatial coordinates and optionally, cell type annotation priors. Subsequently, gsMap identifies homogeneous spots for each spot on the basis of their cosine similarity in the embeddings, to form a microdomain. Each spot is considered in turn as a focal spot, and the specificity score for each gene in each focal spot is computed by dividing the average rank of a gene's expression level within the microdomain by its average rank across the entire ST section. *D*, microdomain of spots; *F*, gene expression specificity; *G*, spot spatial graph; *R*, rank; *X*, gene expression matrix; *Z*, embeddings. **b**, The GSSs of each spot are then mapped to SNPs on the basis of their distance to TSSs and SNP-to-gene linking maps, resulting in a unique set of SNP annotations for each spot. For the SNP GSS annotations of each spot, gsMap uses S-LDSC to assess whether SNPs with higher GSSs are enriched for heritability for the trait of interest. LD, linkage disequilibrium. **c**, To quantify the significance of a spatial region's association with the trait, gsMap utilizes the Cauchy combination test to aggregate *P* values of spots within that spatial region.

both gene expression patterns and spatial positions. The gene specificity scores (GSSs) of each spot are computed by aggregating information from these homogeneous spots, representing the relative rank of the expression level of each gene in a spot (Fig. 1a). Second, gsMap assigns the GSSs of each spot to SNPs within a window extending 50 kb upstream and 50 kb downstream of each gene's transcribed region, along with SNP-to-gene maps established using epigenomic data[14–16], giving rise to a unique set of SNP GSS annotations for each spot. Treating each spot as an SNP annotation set, gsMap assesses whether SNPs with higher GSSs disproportionately explain a larger proportion of heritability for the trait using the stratified linkage disequilibrium score regression (S-LDSC)[17,18], conditional on the baseline annotations (Fig. 1b). The enrichment *P* value is used to measure the statistical significance of association of a spot with the trait. Finally, to quantify the significance of association of a specific spatial region with a trait, gsMap utilizes the Cauchy combination test[19] to aggregate *P* values of individual spots within that spatial region (Fig. 1c). In essence, gsMap can be considered as a method for genetically informed mapping of complex traits to ST data at cellular resolution.

Validation of gsMap

As a proof of principle, we sought to validate gsMap by corroborating known associations between different tissues and traits. For this validation analysis, we used ST data collected from the late embryo stage, as it covers a comprehensive spectrum of tissues. Owing to the lack of human ST data at the late embryonic stage, we used a mouse dataset from Chen et al.[5], which included 25 different organs at the developmental stage of embryonic day 16.5 (E16.5) (Fig. 2a and Methods). This strategy assumes that gene expression profiles in mice resemble those in humans, an assumption largely supported by previous evidence demonstrating more than 80% correlation in tissue-level expression across genes between mice and humans[20], and more than 75% correlation at the cell type level (Methods and Supplementary Fig. 1). The Chen et al. mouse ST dataset was generated using Stereo-seq, and contains data at 'bin50' resolution, whereby each spot represents a few cells, and single-cell resolution. For robustness, we began by using data at the bin50 resolution. We included publicly available GWAS summary statistics for 110 complex traits (average n = 385,000; Supplementary Table 1 and Supplementary Note, section 4) in this analysis. Our gsMap successfully recapitulated known associations between different organs and traits[8,21]. For example, intelligence quotient (IQ) was mapped to spots located in the brain, mean corpuscular haemoglobin concentration (MCHC) was associated with spots in the liver, and height was mapped to various tissues, with cartilage and its primordium showing the highest relevance (Fig. 2b). The aggregated tissue-level association *P* values, obtained using the Cauchy combination test, confirmed these observations (Fig. 2c and Supplementary Table 2). Sensitivity analyses suggested that these results were not driven by the few genes with the highest GSS at each spot (Supplementary Fig. 2).

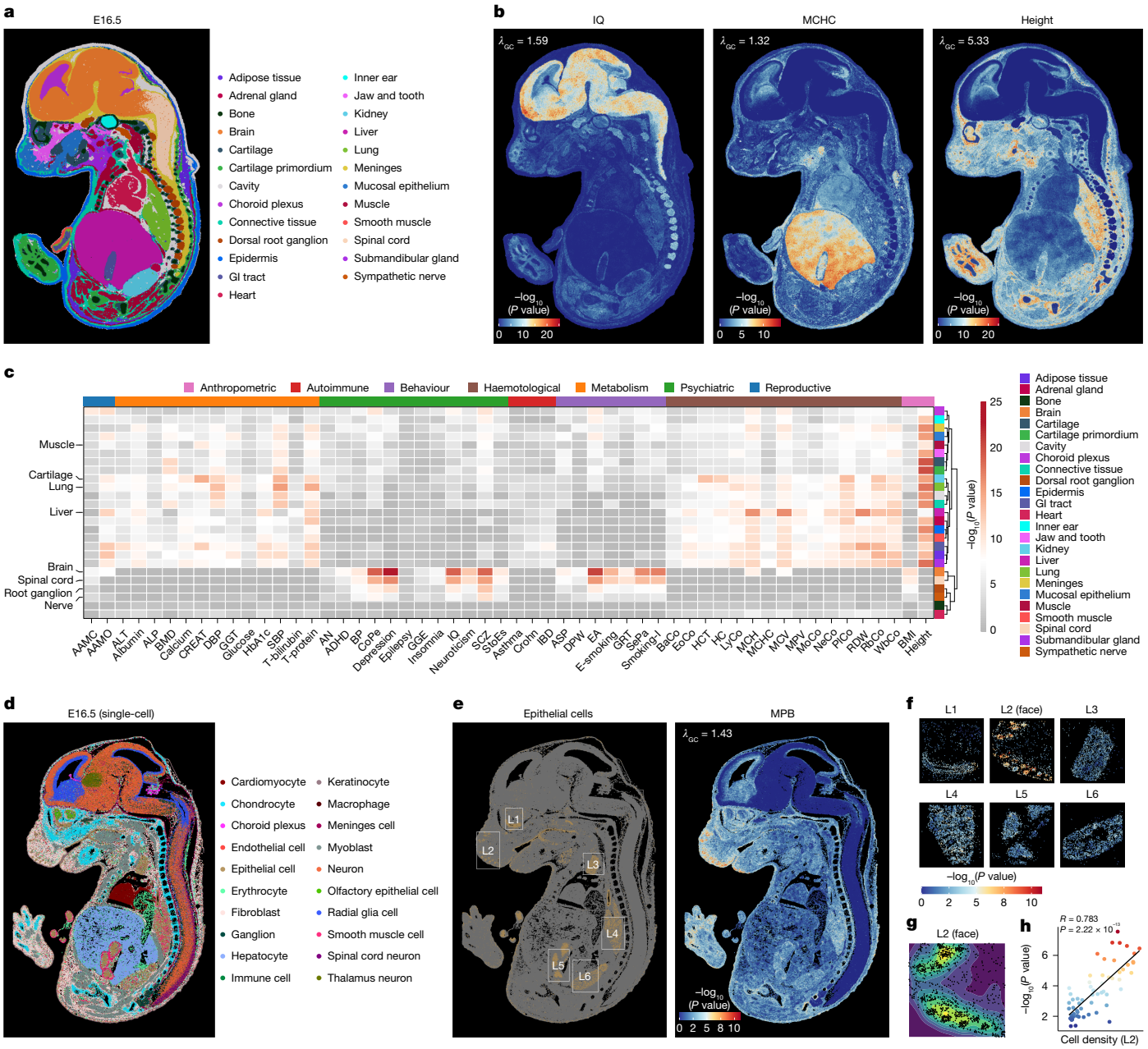

Fig. 2 | Mapping human complex traits to mouse embryo. a, Mouse E16.5 embryonic ST data at bin50 resolution[5], with spots coloured by tissue types. GI, gastrointestinal. **b**, gsMap results for IQ, MCHC and height using the mouse E16.5 embryonic ST data, with colours indicating the significance of the association. The genomic inflation factor (λ_{GC}), serves as an indicator of GWAS statistical power. **c**, Tissue–trait associations, with rows representing tissue types and columns representing traits. Colours indicate the significance of the association. Trait abbreviations are listed in Supplementary Table 1. **d**, Mouse E16.5 embryonic ST data at single-cell resolution, with spots coloured by cell type[5]. **e**, Left, distribution of epithelial cells in the mouse E16.5 embryo, with white rectangles showing six spatial regions. Brown dots represent epithelial cells. Right, gsMap results for MPB, with spots coloured by the significance of the association. **f**, gsMap results for MPB in the six spatial regions. **g**, Densities of epithelial cells in the face (L2) region. The gradient colours from blue to yellow represent cell density from low to high. Black dots represent epithelial cells. **h**, Correlation between epithelial density and the significance of the association of epithelial cells with MPB in the face region. Epithelial densities were estimated as the smoothed relative count of epithelial cells within 100 grids, and the significance of epithelial–MPB associations for each grid were estimated using the interpolate method. The *x* axis shows epithelial density and the *y* axis shows the significance of epithelial–MPB association. Data points represent grids, coloured by significance of the association. The black line indicates the regression line; *P* value from a two-sided *t*-test ($n = 100$).

We have also applied gsMap to ST data from an intact human embryo at Carnegie stage 8 (CS8)[7]. Despite the incomplete formation of organs at this developmental stage, gsMap successfully mapped traits to their respective organ progenitors. For example, IQ was mapped to the ectoderm ($P = 1.5 \times 10^{-6}$), the progenitor of the brain, whereas MCHC was mapped to the endoderm ($P = 1.5 \times 10^{-9}$), the progenitor of the liver (Extended Data Fig. 1 and Supplementary Table 3).

To validate the reliability of the identified associations between traits and spots, we simulated four different null scenarios with varying levels of heritability and polygenicity, based on real genotype data from 100,000 unrelated individuals of European ancestry from the UK Biobank[22] (Methods). In these scenarios, causal variants were either randomly distributed or concentrated in specific genomic regions but were not enriched in genes with spatially dependent expression.

Under all null scenarios, the false discovery rate (FDR) of gsMap was well controlled, as it did not identify any spots showing significant associations at FDR < 0.05 (Extended Data Fig. 2 and Supplementary Figs. 3 and 4).

To showcase the capability of gsMap in spatially resolved mapping of cells to a trait, we applied it to mouse embryonic ST data at single-cell resolution[5] (Fig. 2d and Methods). Taking male pattern baldness (MPB) as an example, we identified an association between MPB and epithelial cells in the face region (Fig. 2e). Notably, the MPB-associated epithelial cells were not randomly distributed but tended to cluster together spatially (Fig. 2f). The significance level of the cells' association with MPB was strongly correlated ($r = 0.78$ and $P = 2.2 \times 10^{-13}$) with the density of epithelial cells (Fig. 2g,h). The tight spatial assembly of epithelial cells suggested that they may form hair follicles, supported by the expression profile of the hair follicle-associated marker genes *KRT15*, *KRT5* and *KRT17* (Supplementary Fig. 5).

As mentioned above, established methods for integrating GWAS with scRNA-seq data, such as single-cell disease relevance score (scDRS)[9], can be repurposed for ST data, even though they do not contain spatial coordinate information. We compared gsMap and scDRS using both simulated and real GWAS datasets (Supplementary Figs. 6 and 7 and Supplementary Note, section 6).

Mapping human traits to mouse brain

We first applied gsMap to map human complex traits to brain regions, owing largely to the abundant availability of brain ST data, even though the majority are not derived from human samples. To ensure statistical power, we included 30 distinct brain-related traits with large GWAS sample sizes (average $n = 315{,}000$) in our analyses, which cover cognition, emotion and behaviour. Owing to the lack of human whole-brain ST data, we began by integrating GWAS summary statistics with mouse brain ST data and focused primarily on the evolutionarily conserved brain regions to ensure the broad extrapolation of the results. We processed adult mouse hemibrain coronal section ST data from Chen et al.[5], which comprised 50,140 cells from 14 brain regions and 13 cell types (Fig. 3a). We began by assessing the association of an entire brain region with a trait by aggregating the *P* values of individual cells in each brain region using the Cauchy combination test (Fig. 3b). We observed that the cortex showed the highest relevance to most traits, such as IQ ($P = 9.8 \times 10^{-15}$), schizophrenia (SCZ) ($P = 1.7 \times 10^{-17}$) and depression ($P = 1.0 \times 10^{-18}$). The second-highest associated brain regions varied across traits: IQ was mapped to the hippocampus cornu ammonis area 1 (CA1) ($P = 7.2 \times 10^{-13}$), SCZ to the hippocampus CA1 ($P = 4.4 \times 10^{-14}$) and depression to the midbrain ($P = 1.1 \times 10^{-15}$).

As brain regions contain various cell types, we explored their contributions to the brain region–trait associations by assessing whether a higher proportion of a specific cell type correlates with increased significance in brain region–trait association. We discovered that, on average across traits, Glu-neurons showed the strongest contributions to the brain region–trait associations (median $r = 0.73$) among all cell types. For instance, the correlation between the significance of the association of a brain region with SCZ and its Glu-neuron proportion was 0.80 ($P = 6.3 \times 10^{-4}$) (Fig. 3c–e). Such a relationship was replicated using brain sagittal section ST data from the mouse E16.5 embryo (Extended Data Fig. 3). However, there were two outliers, Parkinson's disease and Alzheimer's disease. We observed that brain regions with higher proportions of dopaminergic neurons (DA-neurons) exhibited stronger associations with Parkinson's disease ($r = 0.81$ and $P = 4.9 \times 10^{-4}$; Fig. 3e). Specifically, the substantia nigra/ventral tegmental area (SN/VTA), which is known to have the highest abundance of DA-neurons, demonstrated the highest relevance to Parkinson's disease ($P = 5.2 \times 10^{-5}$; Extended Data Fig. 4). This finding was in line with previous neurological studies that showed a notable impairment in the SN/VTA region among individuals with Parkinson's disease[23,24].

Having noted the important role of Glu-neurons in most of the analysed traits, we proceeded to explore whether the associated Glu-neurons were distributed in distinct patterns for different traits. Recognizing that direct comparison of gsMap results across traits might be confounded by variation in GWAS statistical power, we used odds ratio (OR), calculated as the ratio of trait-associated Glu-neurons to non-associated ones in a specific region, divided by that ratio in all other regions (Methods). Our analysis focused on SCZ, cognitive traits (such as IQ) and mood traits (such as depression), as Glu-neurons significantly contributed to the association of these traits with brain regions (Fig. 3e), and their GWAS data were sufficiently powered ($\lambda_{GC} > 1.3$). We found that, beyond the cortex, Glu-neurons in the hippocampus CA areas were strongly associated with cognitive traits (for example, OR = 1.5 and $P = 4.3 \times 10^{-25}$ for IQ), while Glu-neurons associated with mood traits tended to be distributed in the midbrain (for example, OR = 6.7 and $P = 7.9 \times 10^{-221}$ for depression; Fig. 3f,g). Notably, although SCZ encompasses both cognitive and mood symptoms, we found that Glu-neurons associated with SCZ exhibited a similar spatial pattern to those associated with cognitive traits and are particularly enriched in the hippocampus CA areas (OR = 4.5 and $P = 7.6 \times 10^{-158}$; Fig. 3g).

Together, our results revealed that: (1) among the brain regions, the cortex exhibited the strongest association with most traits, but Parkinson's disease was significantly associated only with the SN/VTA; (2) Glu-neurons contributed substantially to the associations between traits and brain regions; (3) Glu-neurons distributed in different brain regions displayed different associations with traits. Glu-neurons distributed in the hippocampus CA areas showed strong associations with cognitive traits and SCZ, whereas those in the midbrain exhibited strong associations with mood disorders such as depression.

Trait-associated neurons in mouse hippocampus

Having shown that the proportion of trait-associated Glu-neurons varied across different brain regions, we next sought to explore whether these neurons exhibit specific patterns of spatial distribution within individual brain regions. We began by focusing on the hippocampus cornu ammonis area 1 (CA1), as the spatial structure of the CA1 region is relatively simple, and previous studies[25,26] have suggested that the electrophysiological properties of pyramidal neurons in CA1 exhibit variation across their spatial positions. Cells within the CA1 region are densely arranged along three spatial axes: the proximal–distal (P–D) axis, the dorsal–ventral (D–V) axis and the deep–superficial (D–S) axis (Fig. 4a). As the brain ST data used in this study correspond to a coronal section, tracking the spatial distribution of Glu-neurons along the P–D axis was unfeasible. Consequently, our investigation focused on the spatial distribution of Glu-neurons along the D–V and D–S axes.

First, along the D–V axis, we observed that Glu-neurons closer to the CA1 dorsal side showed stronger associations with the traits (Supplementary Fig. 8), and this trend was particularly evident for SCZ ($r = -0.51$ and $P = 3.5 \times 10^{-190}$; Fig. 4b,c). We replicated this decline in association strength along the D–V axis between Glu-neurons and SCZ using a mouse brain multiplexed error-robust fluorescence in situ hybridization (MERFISH) ST dataset, including both coronal and sagittal sections from multiple individuals[27] (Extended Data Fig. 5). To investigate the underlying mechanisms, we conducted two expression association analyses to identify genes whose expression levels in Glu-neurons were associated with their positions along the D–V axis, and genes whose expression levels in Glu-neurons were associated with their relevance to SCZ (Methods). The *z*-statistics from these two analyses showed a strong correlation ($r = 0.78$ and $P < 5 \times 10^{-324}$) with *HPCA* (encoding a calcium-binding protein), *PPP3CA* (encoding a calcineurin subunit) and *ATP2B1* (encoding a calcium-transporting protein) emerging as the top three genes prioritized in both analyses (Fig. 4d). A subsequent gene ontology (GO) term enrichment analysis revealed that the identified

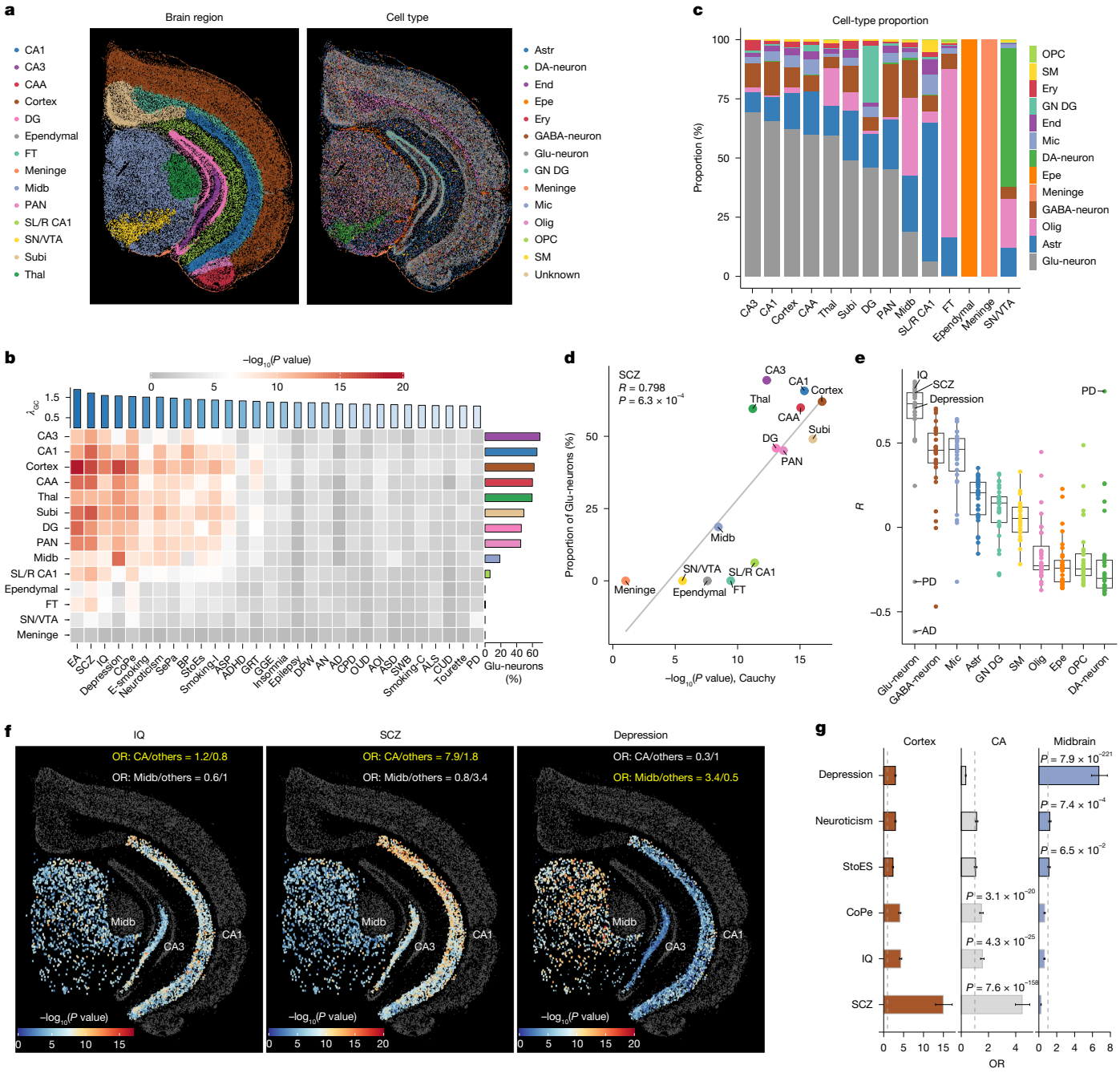

Fig. 3 | Mapping human complex traits to adult mouse brain. a, Adult mouse brain ST data[5], with spots coloured by brain region (left) or cell type (right). **b**, Brain region–trait associations, with colours indicating the significance of the association. Rows represent brain regions and columns represent traits. The right bar shows the proportion of Glu-neurons per brain region and the top bar represents λ_{GC}, which serves as an indicator of GWAS statistical power. Abbreviations for brain region and cell types are listed in Supplementary Note, section 5. **c**, Cell type proportions across brain regions. **d**, Correlation between the significance of a brain region's association with SCZ (*x* axis) and its proportion of Glu-neurons (*y* axis). The grey line represents the regression line; *P* value from a two-sided t-test ($n = 14$). **e**, Correlation between the significance of association with a trait and the proportion of a cell type across brain regions ($n = 30$). The *x* axis displays different cell types and the *y* axis shows the Pearson correlation coefficient. Points represent traits and are coloured by cell type. In each box, the central line denotes the median, notches represent the 95% confidence interval, the box indicates the interquartile range and whiskers extend up to 1.5 times the interquartile range. AD, Alzheimer's disease; PD, Parkinson's disease. **f**, gsMap results for IQ, SCZ and depression in the midbrain and CA regions. Each point represents an individual Glu-neuron, with colour indicating the significance of its association with a trait. **g**, ORs of cortex (left), CA (middle) and midbrain (right). Error bars represent the 95% confidence interval, with the centre indicating the OR. *P* values from a two-sided Chi-square test ($n = 19{,}598$). Bar plots ensure visibility of small-range error bars (individual data points are not shown). CoPe, cognitive performance.

genes were enriched in pathways related to calcium and ion transport (Fig. 4e).

The spatial scale of the D–S axis is narrow, yet we also observed heterogeneity among Glu-neurons along this axis. Leveraging gsMap, we found that Glu-neurons closer to the CA1 superficial side exhibited stronger associations with depression ($r = 0.18$ and $P = 2.7 \times 10^{-20}$; Fig. 4f). This finding aligns with a recent study suggesting that manipulating CA1 superficial neurons, but not deep neurons, could ameliorate depressive-like behaviours in mice[28]. Motivated by the result above showing that Glu-neurons in the midbrain were highly

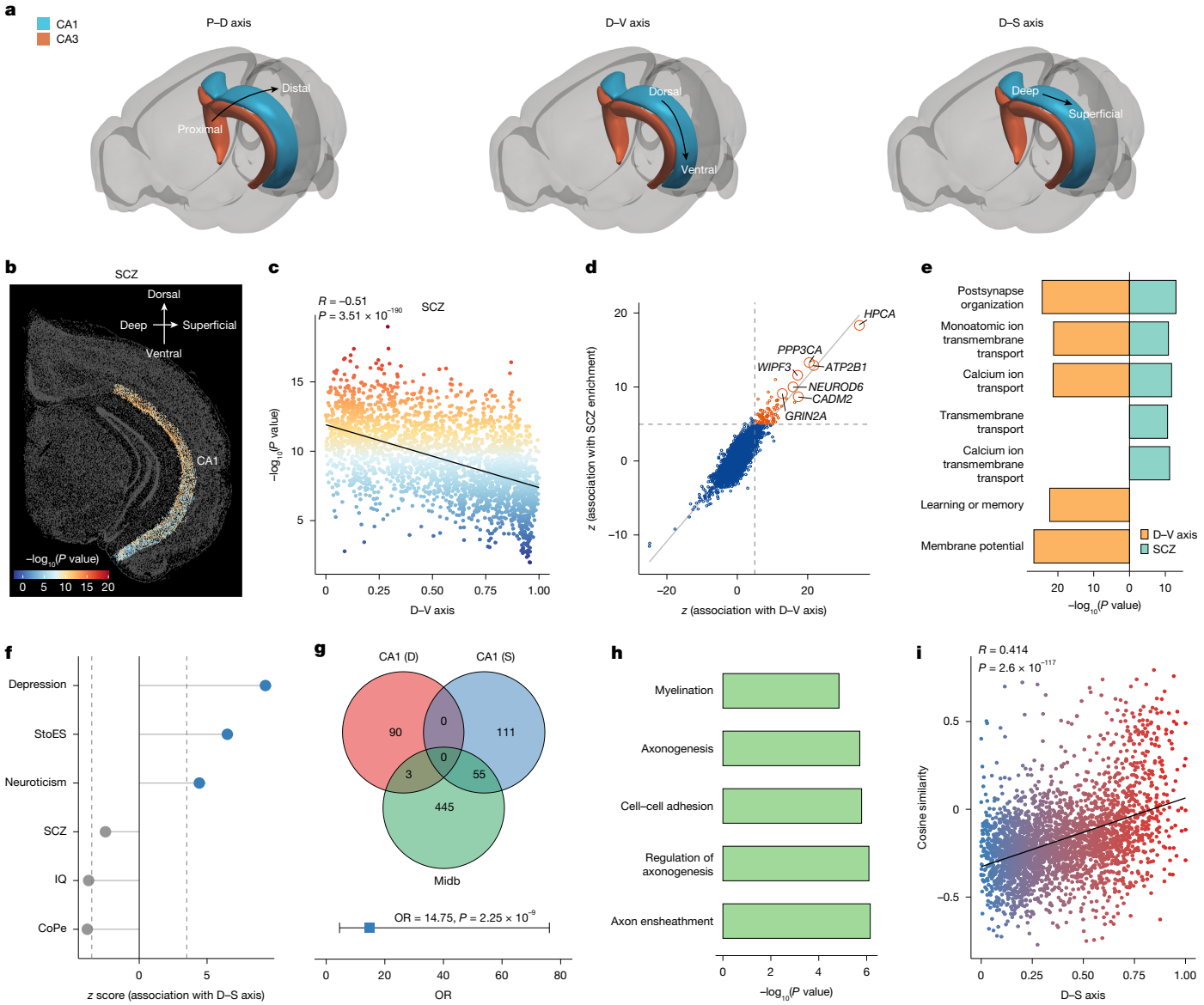

Fig. 4 | Trait-associated Glu-neurons in mouse hippocampus. a, Schematic of the three spatial axes of the mouse hippocampus. **b**, gsMap results of SCZ in CA1, with colours indicating the significance of the association. **c**, Correlation between the significance of the association of a Glu-neuron with SCZ and its spatial position along the CA1 D–V axis, with cells coloured by the significance of the association. The *P* value for the black regression line is from a two-sided *t*-test ($n = 2{,}824$). **d**, *z*-Statistics from correlation analyses. The *x* axis shows the *z*-statistic for correlation between gene expression levels in Glu-neurons and their spatial positions along the D–V axis and the *y* axis shows the significance of their association with SCZ. Genes with an FDR < 0.01 are highlighted in orange. **e**, GO term enrichment of genes whose expression levels were correlated with the spatial positions of Glu-neurons along the D–V axis ($n = 241$) or significance of the association with SCZ ($n = 100$). **f**, *z*-Statistic for the correlation between the significance of the associations of Glu-neurons with traits and spatial positions along the CA1 D–S axis. Dashed lines represent the threshold at FDR = 0.01. **g**, Top, overlap of genes that are highly expressed in the CA1 deep side, superficial side and midbrain. Bottom, OR of contrasting genes that are highly expressed in both the midbrain and CA1 superficial side versus those that are highly expressed in the midbrain and CA1 deep side. The error bar represents the 95% confidence interval, with the centre line indicating the OR ($n = 259$). **h**, GO term enrichment of genes highly expressed in both the midbrain and CA1 superficial side ($n = 55$). **i**, Correlation between CA1 Glu-neuron positions along the D–S axis (*x* axis) and gene expression cosine similarity with midbrain Glu-neurons (*y* axis), with cells coloured by their position along the D–S axis. The *P* value for the black regression line is from a two-sided *t*-test ($n = 2{,}824$). *P* values in **e**, **g** and **h** are from a two-sided Chi-square test.

relevant to depression (Fig. 3g), we further investigated associations between Glu-neurons in the CA1 superficial side and those in the midbrain. We found that genes highly expressed (at FDR < 0.05) in the midbrain showed a greater overlap with genes highly expressed in the CA1 superficial side than those in the CA1 deep side (55 versus 3 genes, OR = 14.75, $P = 2.25 \times 10^{-9}$; Fig. 4g). GO term enrichment analysis indicated that genes highly expressed in both midbrain and the CA1 superficial side were enriched in pathways related to axonogenesis and neuron ensheathment (Fig. 4h). The transcriptomic similarities of Glu-neurons between the CA1 and the midbrain increased along the CA1 D–S axis ($r = 0.41$ and $P = 2.6 \times 10^{-117}$; Fig. 4i). These results suggested that there are functional overlaps between Glu-neurons in the midbrain and those at the CA1 superficial side.

In summary, our results revealed spatially patterned distributions of trait-associated Glu-neurons in the hippocampus CA1 region. Glu-neurons closer to the CA1 dorsal side showed stronger associations with SCZ, and showed increased expression of calcium signalling and regulation genes. Glu-neurons closer to the CA1 superficial side exhibited stronger associations with depression, and showed increased expression of axonogenesis-related genes.

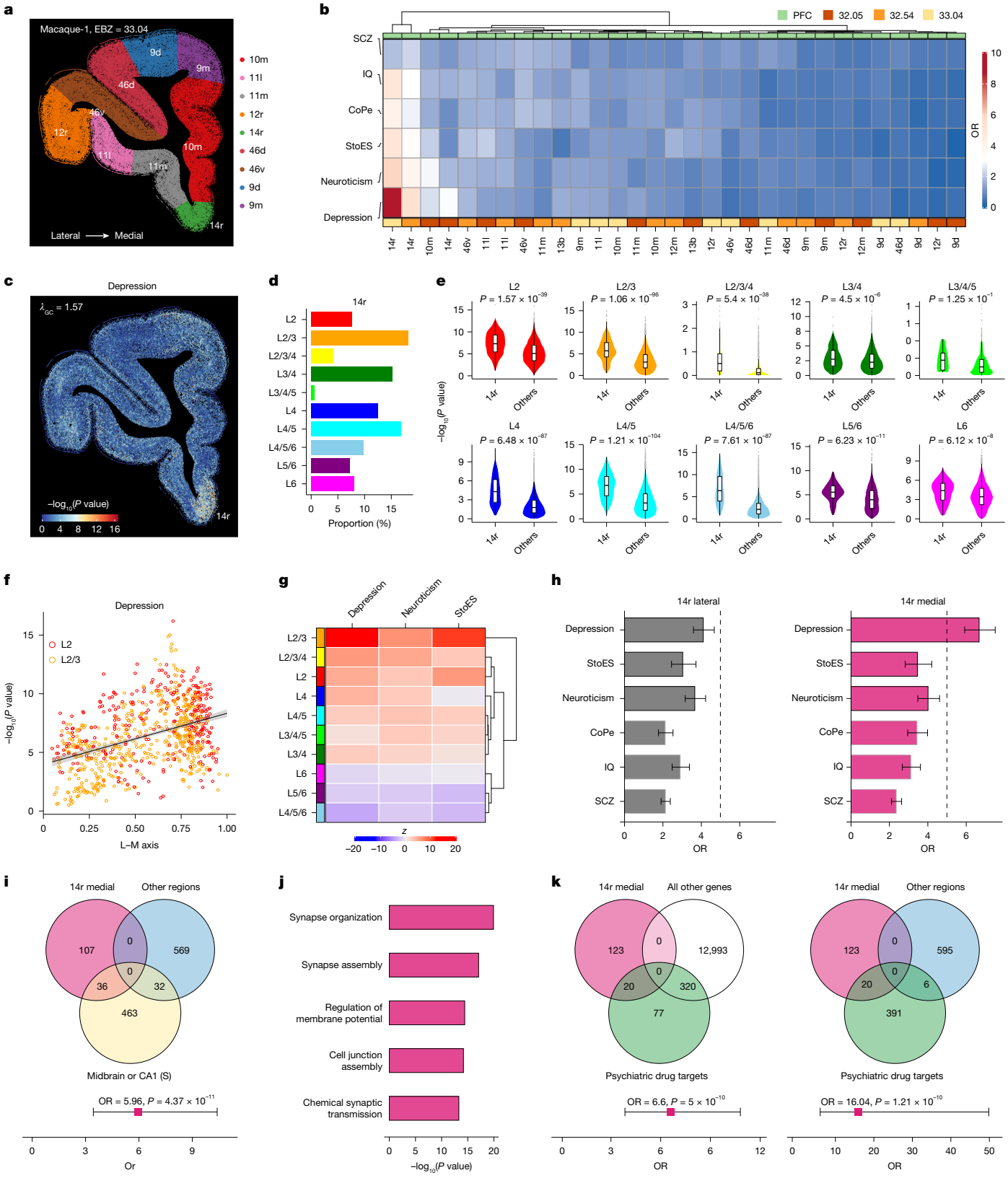

Fig. 5 | See next page for caption.

Mapping human traits to macaque cortex

The analyses above with the adult mouse ST data focused on hippocampus and midbrain, which are evolutionarily conserved across different mammalian species in terms of their spatial structures and biological functions[29–31]. To extend our analyses to an evolutionarily more advanced brain area—the cerebral cortex[32]—we faced challenges owing to the functional and structural differences between human and mouse

Fig. 5 | Trait-associated Glu-neurons in macaque PFC. a, Macaque PFC ST data, with cells coloured by cortical regions. EBZ denotes the position of the section. **b**, ORs of Glu-neurons, with bottom annotations indicating ST sections. **c**, gsMap results for depression, with cells coloured by the significance of the association. **d**, Proportions of Glu-neuron subtypes in 14r. **e**, gsMap results for Glu-neuron subtypes in 14r and other regions. Two-sided Wilcoxon rank-sum test *P* values are shown in each graph ($n = 88{,}857$). The central line denotes the median, notches represent the 95% confidence interval, the box indicates the interquartile range, and whiskers extend up to 1.5 times the interquartile range. **f**, Correlation between the L2 (L2/3) Glu-neuron positions along the L–M axis (*x* axis) and the significance of the association with depression (*y* axis). Points denote individual Glu-neurons, and are coloured by subtype. The black line is the regression line, with the shaded area indicating the 95% confidence interval. **g**, *z*-Scores for the correlation between the significance of the association with Glu-neuron traits and their positions along the L–M axis. Rows correspond to Glu-neuron subtypes and columns represent traits. **h**, ORs of Glu-neurons in the 14r lateral (left, $n = 1{,}344$) and medial (right, $n = 1{,}340$) side. Bar plots ensure visibility of small-range error bars (individual data points are not shown). The dashed line represents the OR of 14r. **i**, Fold enrichment of genes that are highly expressed in the mouse midbrain or CA1 (S) and macaque PFC 14r medial side ($n = 143$), compared with other PFC regions ($n = 601$). **j**, GO term enrichment of genes that are highly expressed in the 14r medial side ($n = 143$). **k**, Fold enrichment of genes that are highly expressed in the 14r medial side ($n = 143$) in psychiatric drug targets, compared with all other detected genes (left, $n = 13{,}313$) or genes highly expressed in other PFC regions (right, $n = 601$). Error bars in **h**,**i**,**k** represent the 95% confidence interval, with the centre indicating the OR. *P* values from a two-sided Chi-square test.

cortices[32–34]. The currently available human cortical ST dataset[13] is limited in coverage and resolution, as it encompasses only a small portion of the dorsolateral prefrontal cortex (DLPFC). We therefore utilized the macaque cerebral cortical ST dataset from Chen et al.[35], which more closely resembles the human cortex and provides single-cell resolution across 143 cortical regions from three adult macaques (Supplementary Tables 4 and 5).

The availability of serial cortical sections in the macaque ST data provided an additional opportunity to validate the robustness of gsMap (Extended Data Fig. 6a). The gsMap results showed remarkable consistency between adjacent ST sections (for example, median $r = 0.92$ for SCZ; Extended Data Fig. 6b and Supplementary Figs. 9 and 10). We next compared gsMap results for SCZ between spatially matched ST sections from different biological replicates. These comparisons also showed strong consistency, with median *r* values of 0.84 using the macaque cortical ST dataset and 0.83 using the mouse embryonic ST dataset (Extended Data Fig. 7). In addition, although single-cell resolution human whole cortex data were unavailable, we examined the consistency between gsMap results in human DLPFC and macaque prefrontal cortex (PFC). We chose to use the macaque PFC owing to the ambiguity in the sampled positions of the human DLPFC, which made it difficult to accurately select the matched cortical lobe from the macaque (Methods). The gsMap results based on the macaque PFC ST data (Stereo-seq) were strongly correlated ($r = 0.51$, $P = 8.6 \times 10^{-8}$) with those based on the human DLPFC ST data (10X Visium), despite the discrepancies including differences in ST platform and definition of cortical lobe (Extended Data Fig. 8 and Supplementary Fig. 11). Given the consistency observed, we mapped 30 human brain-related traits to ST sections across the entire macaque left cerebral cortex at a spatially resolved single-cell resolution. These mapping results are available at https://yanglab.westlake.edu.cn/gsmap.

To systematically analyse the spatial association maps between brain-related traits and cortical cells, we began by estimating the correlation between pairs of traits regarding their associations with cells across the cerebral cortex, hereafter referred to as cell relevance correlation (CRC). We observed that SCZ clustered with other cognitive traits (for example, cognitive performance), while mood traits formed another cluster (Extended Data Fig. 6c). This result remains consistent after adjusting for GWAS statistical power and aligns with our findings using the mouse brain ST data (Figs. 3 and 4 and Supplementary Figs. 12 and 13), indicating differences in relevant brain regions between cognitive and mood traits. Notably, CRC between two traits could differ substantially from their genetic correlation (Extended Data Fig. 6d). For instance, whereas the genetic correlation (r_G) between glycated haemoglobin (HbA1c) and high-density lipoprotein (HDL) was negative ($r_G = -0.18$ and $P = 1.6 \times 10^{-11}$), their CRC was positive (CRC = 0.79 and $P < 5.0 \times 10^{-324}$), owing to their shared associations with cells distributed in the liver (Supplementary Fig. 14). SCZ is a complex psychiatric disorder that involves a combination of cognitive, mood and behavioural symptoms, and is typically not classified solely as a cognitive or mood disorder. However, in our study, we found a stronger CRC of SCZ with cognitive traits (for example, CRC = 0.72 between cognitive performance and SCZ) across cortex cells (Extended Data Fig. 6e) compared with mood traits (for example, CRC = 0.55 between depression and SCZ). This result indicated widely shared cells and cortical regions between SCZ and cognitive performance, suggesting that impairment in the brain areas associated with cognition might be a major pathological change in individuals with SCZ.

Trait-associated neurons in macaque PFC

Leveraging the spatially resolved cortex cell–trait association maps generated above, we investigated the spatial distributions of trait-associated neurons in the adult macaque PFC, considering that previous studies have indicated significant roles of the PFC in emotion and cognition[36–38] (Fig. 5a). Neurons in the other cortical lobes are also crucial; however, owing to space limitations, we focused on the PFC lobe and presented results of other cortical lobes on our interactive website.

We first explored the distributions of trait-associated Glu-neurons in different PFC regions. We found that Glu-neurons in the PFC 14r region (gyrus rectus) exhibited a strong association with depression (OR = 5.3, $P = 5.2 \times 10^{-123}$; Fig. 5b,c), and these results remained consistent when using data from adjacent PFC ST sections (Supplementary Fig. 15). This robust association was evident across most subtypes (layers) of Glu-neurons, except for rare Glu-neurons annotated as L3/4/5 (Fig. 5d,e and Supplementary Fig. 16). Furthermore, we found that the associations between traits and Glu-neurons in the PFC 14r region correlated with their local spatial distributions. Along the lateral–medial (L–M) axis of the 14r region, we observed an increasing relevance of Glu-neurons to mood disorders, particularly within the superficial cortex layers (such as L2 and L3; Fig. 5f,g). When dividing the 14r region into lateral and medial sides, depression (lateral side OR = 4.1, $P = 2.9 \times 10^{-78}$; medial side OR = 6.7, $P = 3.6 \times 10^{-169}$) exhibited more pronounced associations with Glu-neurons in the medial side (Fig. 5h). To investigate the underlying biological mechanisms, we compared gene expression levels of Glu-neurons in the medial side of the PFC 14r region with those in the other PFC regions and identified 143 highly expressed genes (at FDR < 0.05) in the 14r medial side (Supplementary Fig. 17). GO term enrichment analysis revealed that these genes were enriched in pathways related to synapse organization and cell junction assembly (Fig. 5j). Recalling the findings above that Glu-neurons distributed in both the midbrain and CA1 superficial side showed high relevance to depression (Figs. 3 and 4), we also assessed the overlap between these genes and the genes highly expressed in midbrain or CA1 superficial side in the mouse brain ST data. This overlap was significantly higher compared with the overlap with genes highly expressed in the other PFC regions (OR = 6.0, $P = 4.4 \times 10^{-11}$; Fig. 5i). Moreover, genes highly

expressed in the midbrain and CA1 superficial side were enriched in pathways of axonogenesis and cell adhesion (Fig. 4i), which are closely interconnected with pathways of synapse organization and cell junction assembly identified in the PFC 14r medial side. These pathways collectively contribute to neural plasticity, a fundamental mechanism of neuronal adaptation to environmental stimuli, which might be disrupted in individuals with depression[39–41].

Next, to demonstrate the clinical value of the PFC 14r region prioritized by gsMap, we conducted an enrichment analysis to explore whether genes highly expressed in the PFC 14r region are enriched in target genes of approved or launched psychiatric drugs. We collected 417 psychiatric drug target genes from the Drug Repurposing Hub and DrugBank database[42,43] (Methods). Genes that were highly expressed in the PFC 14r region showed significant enrichment in psychiatric drug targets, compared with genes that were highly expressed in the other PFC regions (OR = 5.2, $P = 1.6 \times 10^{-10}$) or all other genes captured in the macaque ST data (OR = 5.1, $P = 3.7 \times 10^{-4}$; Supplementary Fig. 18). This enrichment was even more pronounced for genes highly expressed in the medial side of the PFC 14r region (OR = 16.0, $P = 2.2 \times 10^{-10}$; Fig. 5k). These genes also showed substantial overlaps with genes identified by commonly used gene prioritization methods for complex traits (Supplementary Fig. 19 and Methods). Consistently, we observed that cells that were distributed in the PFC 14r medial side exhibited the highest drug module score compared with those that were distributed in other PFC regions (Extended Data Fig. 9). We further explored drugs whose target genes were enriched in genes that were highly expressed in the PFC 14r medial side compared with all other genes (Supplementary Note, section 7 and Supplementary Table 6).

Together, our results revealed spatially patterned associations between Glu-neurons and traits in the PFC lobe. We found that Glu-neurons near the medial side of the PFC 14r (gyrus rectus) region were strongly associated with depression, and genes that were highly expressed in this area were enriched in neural plasticity-related pathways and targets of psychiatric drugs.

Discussion

Here we introduced gsMap, which integrates cellular gene expression profiles, cell spatial coordinates, SNP-to-gene linking maps and GWAS summary data to spatially map cells to human complex traits. The gsMap method has been implemented in a Python package and is freely available at https://github.com/JianYang-Lab/gsMap. Through extensive benchmark analyses with real ST and both real and simulated GWAS datasets, we demonstrated that gsMap was accurate, robust and powerful in spatially aware identification of associations between traits and cells (Supplementary Figs. 20–25). By applying gsMap to high-resolution brain ST datasets, we generated trait–brain maps that detail associations with 30 complex traits at spatially resolved single-cell resolution. These maps cover both evolutionarily conserved brain regions (such as hippocampus) and advanced brain regions (such as cerebral cortex), and various complex traits related to cognition, emotion and behaviour, and several of our findings hold clinical value (Supplementary Note, section 8). We have developed an interactive web tool (https://yanglab.westlake.edu.cn/gsmap) to visualize and download these trait–brain association maps. Although we have primarily used gsMap as a genetic analysis tool for this study, it can be integrated into ST data analysis toolkits to explore associations of individual cells with human diseases, providing insights into the disease relevance of spatially patterned human cells for improved diagnosis and treatment, and into the relevance of animal cells to human diseases for better disease modelling. Furthermore, we have provided an option in gsMap to jointly analyse multiple ST sections (Methods) and have demonstrated consistency between the results from separate and joint analyses (Supplementary Fig. 26). Therefore, we recommend the joint analysis mode for better interpretability of gsMap results from ST data obtained from multiple technical or biological replicates.

Cells in the brain are usually assigned to conventional cell types (for example, Glu-neurons) to study their relevance to diseases[10,21,44]. Our results suggest that owing to within-cell type heterogeneity, assigning cells to such cell types only is not sufficient to understand their roles in diseases. For instance, cells of the same conventional cell type in the brain exhibit a wide heterogeneity regarding their relevance to traits or diseases, and such heterogeneity is correlated with their spatial distributions (Figs. 3–5). Therefore, using spatial context annotations to capture intra-cell type heterogeneity not only allows for mapping of the spatial distribution of trait-associated cells within cell types, but also enhances the power to detect trait-associated tissues or cell types (Supplementary Figs. 20 and 21). Our findings, in conjunction with previous morphology, electrophysiology and RNA-sequencing studies[29,45–48], indicate that spatially patterned within-cell type heterogeneity might be the fundamental organization rule for cells in the mammalian brain (Supplementary Note, section 9).

Another question is whether gsMap relies on the assumption of spatial context-dependent expression quantitative trait locus (eQTL) effects. Context-dependent eQTL effects are often detected on the basis of gene expression levels that are standardized within each context, and findings have consistently shown that most eQTLs are not context-dependent[49–51]. However, even in the absence of context-dependent eQTL effects for the standardized expression levels, the effect of the eQTL variant on a complex trait, as mediated by different cell groups, can differ owing to differences in the variance of raw expression levels across cell groups (Extended Data Fig. 10 and Supplementary Note, section 10). Exploring spatial context-dependent genetic regulation of gene expression would require population-scale ST data, which are currently not available. An alternative approach would be to deconvolute the abundances of spatial domains in bulk samples, analogous to the deconvolution of cell-state abundances[52], followed by an interaction model (spatial domain-by-genotype interaction) to detect spatially dependent genetic effects on gene expression.

We note several limitations in our study, which could serve as potential avenues for future research. First, owing to limitations in the presently available human ST data, we relied on brain ST data obtained from mice and macaques to spatially map brain cells associated with human complex traits. Despite the replication of our findings across diverse ST datasets and the demonstration of consistent gsMap results across mouse, macaque and human data, the use of non-human ST data inevitably leads to a reduction in statistical power owing to inherent differences between humans and these animal models, although the use of GWAS summary data from large-scale studies may partially offset this power loss. Given the rapid development of spatial omics technologies and the reduction in associated costs[3,4,53], we anticipate the generation of extensive, high-quality spatial omics data using human tissues in future studies. These datasets would serve as valuable resources for further validating our results and making novel discoveries that cannot be achieved using non-human ST data. Second, associations between traits and cells identified by gsMap do not imply a causal relationship. Because of the correlation of gene expression profiles among cells, it is possible for cells that do not biologically contribute to a trait to be identified as being associated with the trait. For example, we detected associations of root ganglion cells with SCZ using the mouse embryonic ST data, which might be caused by the correlated gene expression values between root ganglion cells and brain neurons. Third, this study focused on separately analysing each ST section or jointly analysing multiple anatomically homogeneous sections, leaving the joint analysis of multiple anatomically heterogeneous ST sections for further exploration. Fourth, incorporating gene regulatory networks (for example, pathways)[54] into the GSS calculation could potentially improve the power of gsMap. Finally, the primary focus of this work was to apply

gsMap to explore the spatial distribution of trait-associated cells in the brain, leaving the exploration of other tissues for further investigation.

Online content

Any methods, additional references, Nature Portfolio reporting summaries, source data, extended data, supplementary information, acknowledgements, peer review information; details of author contributions and competing interests; and statements of data and code availability are available at https://doi.org/10.1038/s41586-025-08757-x.

1. Rao, A., Barkley, D., França, G. S. & Yanai, I. Exploring tissue architecture using spatial transcriptomics. *Nature* **596**, 211–220 (2021).
2. Ben-Moshe, S. & Itzkovitz, S. Spatial heterogeneity in the mammalian liver. *Nat. Rev. Gastroenterol. Hepatol.* **16**, 395–410 (2019).
3. Moses, L. & Pachter, L. Museum of spatial transcriptomics. *Nat. Methods* **19**, 534–546 (2022).
4. Tian, L., Chen, F. & Macosko, E. Z. The expanding vistas of spatial transcriptomics. *Nat. Biotechnol.* **41**, 773–782 (2023).
5. Chen, A. et al. Spatiotemporal transcriptomic atlas of mouse organogenesis using DNA nanoball-patterned arrays. *Cell* **185**, 1777–1792.e1721 (2022).
6. Thrane, K., Eriksson, H., Maaskola, J., Hansson, J. & Lundeberg, J. Spatially resolved transcriptomics enables dissection of genetic heterogeneity in stage III cutaneous malignant melanoma. *Cancer Res.* **78**, 5970–5979 (2018).
7. Xiao, Z. et al. 3D reconstruction of a gastrulating human embryo. *Cell* **187**, 2855–2874. e2819 (2024).
8. Finucane, H. K. et al. Heritability enrichment of specifically expressed genes identifies disease-relevant tissues and cell types. *Nat. Genet.* **50**, 621–629 (2018).
9. Zhang, M. J. et al. Polygenic enrichment distinguishes disease associations of individual cells in single-cell RNA-seq data. *Nat. Genet.* **54**, 1572–1580 (2022).
10. Jagadeesh, K. A. et al. Identifying disease-critical cell types and cellular processes by integrating single-cell RNA-sequencing and human genetics. *Nat. Genet.* **54**, 1479–1492 (2022).
11. Qi, T., Song, L., Guo, Y., Chen, C. & Yang, J. From genetic associations to genes: methods, applications, and challenges. *Trends Genet.* **40**, 642–667 (2024).
12. Wang, Y. et al. Sprod for de-noising spatially resolved transcriptomics data based on position and image information. *Nat. Methods* **19**, 950–958 (2022).
13. Maynard, K. R. et al. Transcriptome-scale spatial gene expression in the human dorsolateral prefrontal cortex. *Nat. Neurosci.* **24**, 425–436 (2021).
14. Ernst, J. et al. Mapping and analysis of chromatin state dynamics in nine human cell types. *Nature* **473**, 43–49 (2011).
15. Kundaje, A. et al. Integrative analysis of 111 reference human epigenomes. *Nature* **518**, 317–330 (2015).
16. Nasser, J. et al. Genome-wide enhancer maps link risk variants to disease genes. *Nature* **593**, 238–243 (2021).
17. Finucane, H. K. et al. Partitioning heritability by functional annotation using genome-wide association summary statistics. *Nat. Genet.* **47**, 1228–1235 (2015).
18. Gazal, S. et al. Linkage disequilibrium-dependent architecture of human complex traits shows action of negative selection. *Nat. Genet.* **49**, 1421–1427 (2017).
19. Liu, Y. & Xie, J. Cauchy combination test: a powerful test with analytic p-value calculation under arbitrary dependency structures. *J. Am. Stat. Assoc.* **115**, 393–402 (2020).
20. Breschi, A., Gingeras, T. R. & Guigó, R. Comparative transcriptomics in human and mouse. *Nat. Rev. Genet.* **18**, 425–440 (2017).
21. Skene, N. G. et al. Genetic identification of brain cell types underlying schizophrenia. *Nat. Genet.* **50**, 825–833 (2018).
22. Bycroft, C. et al. The UK Biobank resource with deep phenotyping and genomic data. *Nature* **562**, 203–209 (2018).
23. Alberico, S. L., Cassell, M. D. & Narayanan, N. S. The vulnerable ventral tegmental area in Parkinson's disease. *Basal Ganglia* **5**, 51–55 (2015).
24. Thompson, L., Barraud, P., Andersson, E., Kirik, D. & Björklund, A. Identification of dopaminergic neurons of nigral and ventral tegmental area subtypes in grafts of fetal ventral mesencephalon based on cell morphology, protein expression, and efferent projections. *J. Neurosci.* **25**, 6467–6477 (2005).
25. Dougherty, K. A., Islam, T. & Johnston, D. Intrinsic excitability of CA1 pyramidal neurones from the rat dorsal and ventral hippocampus. *J. Physiol.* **590**, 5707–5722 (2012).
26. Malik, R., Dougherty, K. A., Parikh, K., Byrne, C. & Johnston, D. Mapping the electrophysiological and morphological properties of CA1 pyramidal neurons along the longitudinal hippocampal axis. *Hippocampus* **26**, 341–361 (2016).
27. Zhang, M. et al. Molecularly defined and spatially resolved cell atlas of the whole mouse brain. *Nature* **624**, 343–354 (2023).
28. Sancho-Balsells, A. et al. Cognitive and emotional symptoms induced by chronic stress are regulated by EGR1 in a subpopulation of hippocampal pyramidal neurons. *Int. J. Mol. Sci.* **24**, 3833 (2023).
29. Cembrowski, M. S. & Spruston, N. Heterogeneity within classical cell types is the rule: lessons from hippocampal pyramidal neurons. *Nat. Rev. Neurosci.* **20**, 193–204 (2019).
30. Manns, J. R. & Eichenbaum, H. Evolution of declarative memory. *Hippocampus* **16**, 795–808 (2006).
31. Bergmann, E., Zur, G., Bershadsky, G. & Kahn, I. The organization of mouse and human cortico-hippocampal networks estimated by intrinsic functional connectivity. *Cereb. Cortex* **26**, 4497–4512 (2016).
32. Pembroke, W. G., Hartl, C. L. & Geschwind, D. H. Evolutionary conservation and divergence of the human brain transcriptome. *Genome Biol.* **22**, 52 (2021).
33. Rakic, P. Evolution of the neocortex: a perspective from developmental biology. *Nat. Rev. Neurosci.* **10**, 724–735 (2009).
34. Geschwind, D. H. & Rakic, P. Cortical evolution: judge the brain by its cover. *Neuron* **80**, 633–647 (2013).
35. Chen, A. et al. Single-cell spatial transcriptome reveals cell-type organization in the macaque cortex. *Cell* **186**, 3726–3743.e3724 (2023).
36. Dixon, M. L., Thiruchselvam, R., Todd, R. & Christoff, K. Emotion and the prefrontal cortex: An integrative review. *Psychol. Bull.* **143**, 1033–1081 (2017).
37. Pizzagalli, D. A. & Roberts, A. C. Prefrontal cortex and depression. *Neuropsychopharmacology* **47**, 225–246 (2022).
38. Hare, B. D. & Duman, R. S. Prefrontal cortex circuits in depression and anxiety: contribution of discrete neuronal populations and target regions. *Mol. Psychiatry* **25**, 2742–2758 (2020).
39. Duman, R. S., Aghajanian, G. K., Sanacora, G. & Krystal, J. H. Synaptic plasticity and depression: new insights from stress and rapid-acting antidepressants. *Nat. Med.* **22**, 238–249 (2016).
40. Pittenger, C. & Duman, R. S. Stress, depression, and neuroplasticity: a convergence of mechanisms. *Neuropsychopharmacology* **33**, 88–109 (2008).
41. Liu, B., Liu, J., Wang, M., Zhang, Y. & Li, L. From serotonin to neuroplasticity: evolvement of theories for major depressive disorder. *Front. Cell. Neurosci.* **11**, 305 (2017).
42. Corsello, S. M. et al. The Drug Repurposing Hub: a next-generation drug library and information resource. *Nat. Med.* **23**, 405–408 (2017).
43. Knox, C. et al. DrugBank 6.0: the DrugBank Knowledgebase for 2024. *Nucleic Acids Res.* **52**, D1265–D1275 (2024).
44. Li, Y. E. et al. A comparative atlas of single-cell chromatin accessibility in the human brain. *Science* **382**, eadf7044 (2023).
45. Hunsaker, M. R., Fieldsted, P. M., Rosenberg, J. S. & Kesner, R. P. Dissociating the roles of dorsal and ventral CA1 for the temporal processing of spatial locations, visual objects, and odors. *Behav. Neurosci.* **122**, 643–650 (2008).
46. Kesner, R. P., Hunsaker, M. R. & Ziegler, W. The role of the dorsal CA1 and ventral CA1 in memory for the temporal order of a sequence of odors. *Neurobiol. Learn. Mem.* **93**, 111–116 (2010).
47. Yao, Z. et al. A taxonomy of transcriptomic cell types across the isocortex and hippocampal formation. *Cell* **184**, 3222–3241.e3226 (2021).
48. Matho, K. S. et al. Genetic dissection of the glutamatergic neuron system in cerebral cortex. *Nature* **598**, 182–187 (2021).
49. Qi, T. et al. Identifying gene targets for brain-related traits using transcriptomic and methylomic data from blood. *Nat. Commun.* **9**, 2282 (2018).
50. Mu, Z. et al. The impact of cell type and context-dependent regulatory variants on human immune traits. *Genome Biol.* **22**, 122 (2021).
51. Mostafavi, H., Spence, J. P., Naqvi, S. & Pritchard, J. K. Systematic differences in discovery of genetic effects on gene expression and complex traits. *Nat. Genet.* **55**, 1866–1875 (2023).
52. Song, L., Sun, X., Qi, T. & Yang, J. Mixed model-based deconvolution of cell-state abundances (MeDuSA) along a one-dimensional trajectory. *Nat. Comput. Sci.* **3**, 630–643 (2023).
53. Vandereyken, K., Sifrim, A., Thienpont, B. & Voet, T. Methods and applications for single-cell and spatial multi-omics. *Nat. Rev. Genet.* **24**, 494–515 (2023).
54. Ma, Y. et al. Polygenic regression uncovers trait-relevant cellular contexts through pathway activation transformation of single-cell RNA sequencing data. *Cell Genomics* **3**, 100383 (2023).

Methods

Inclusion and ethics

This study was approved by the Ethics Committee of Westlake University (approval no. 20200722YJ001).

gsMap method

Design principles. To effectively illustrate gsMap, we first summarize its design principles. gsMap utilizes the framework of S-LDSC[17] to assess whether genetic variants, mainly SNPs, located in or near genes specifically expressed in a spot in ST data are enriched for genetic associations with a trait of interest. To precisely estimate gene expression specificity for individual spots, gsMap aggregates information from homogeneous spots, a crucial step given the sparsity and high technical noise in gene expression profiles of individual spots in ST data[12,55]. Using spatial coordinates alone is inadequate to identify homogeneous spots because spatially neighbouring spots may not necessarily belong to the same cell type. Using gene expression profiles alone could also lead to biased identification of homogeneous spots owing to technical noise. To address these limitations, gsMap uses a GNN to learn embeddings that integrate spatial coordinates and gene expression profiles, and then identifies homogeneous spots for each focal spot on the basis of their similarity in the embedding matrix. gsMap then estimates GSSs for each focal spot by aggregating information from its homogeneous spots. Note that although spot embeddings for ST data generated from existing tools[56,57] can be applied in gsMap, to enhance usability of our software tool and improve embedding quality, we developed a built-in GNN model (see below) that incorporates spot annotations when available and uses a graph attention layer (GAT) to prevent over-smoothing during the process of identifying homogenous spots for a focal spot.

Data input. gsMap requires inputs of (1) GWAS summary statistics; (2) sequencing-based ST data comprising transcriptome-wide gene expression profiles and spatial coordinates of individual spots; (3) LD reference data; and (4) optionally, SNP-to-gene linking maps. We noted that the resolution of ST data varies significantly across different platforms, ranging from one spot on sequencing array chips representing a cluster of cells (for example, 10X Visium) to spots at sub-cellular resolution (for example, Stereo-seq). To ensure the robustness of gsMap when handling ST data at sub-cellular resolution, cell segmentation[58] analysis is required, which merges original spots on sequencing array chips into individual cells. For simplicity, we continue to use spots to denote data points in ST data, where one spot represents an individual cell (after cell segmentation analysis) in high-resolution ST platforms or multiple cells in conventional ST platforms.

Processing gene expression data. The gene expression count matrix is log-transformed and normalized according to the library size of each spot. Subsequently, the normalized gene expression matrix is standardized to attain a zero mean and unit variance, and the top h (default, 3,000) highly variable genes (HVGs) are retained. We select HVGs based on the normalized variance of each gene, which adjusts for mean-variance associations, as implemented in Scanpy[59]. The resulting processed gene expression matrix is represented as $X \in \mathbb{R}^{n \times h}$, with n denoting the number of spots and h representing the number of HVGs. To accelerate the training process in the GNN, users can optionally provide a principal component analysis-reduced matrix (default, 300 components). The normalized HVG matrix (or principal component analysis-reduced matrix) serves as the feature matrix in the GNN.

Building a spatial graph of the spots. The spatial coordinates of individual spots are transformed into an undirected graph, denoted as $G = (V, E)$. In this graph, each vertex $v \in V$ represents a spot, and E represents the set of connected edges between spots. For balancing the performance and computational efficiency, gsMap, by default, considers the ten nearest neighbouring spots for each spot, determined by their Euclidean distance in spatial coordinates. The resulting graph can be delineated by the adjacency matrix $A \in \mathbb{R}^{n \times n}$ with n denoting the number of spots. If spots i and j are connected in the graph, $A_{ij} = 1$; otherwise, $A_{ij} = 0$.

Learning embedding matrix. The standardized gene expression matrix X and the adjacency matrix A are then integrated into an embedding matrix $Z \in \mathbb{R}^{n \times m}$, where m represents the number of features (set as 32), using the GAT auto-encoder framework. The advantage of GAT[60] lies in its trainable edge weights among connecting spots, enabling higher weights for spots with analogous gene expression patterns during information aggregation. A detailed description of the graph attention auto-encoder can be found in section 1 of the Supplementary Note.

The loss function of the graph attention auto-encoder in gsMap includes two parts: (1) the mean squared error used for reconstructing gene expression matrix; and (2) the cross-entropy loss used for predicting cell types of spots:

$$L = \gamma\left(\sum_{i=1}^{n}\sum_{g=1}^{h}(x_{ig} - \hat{x}_{ig})^2\right) + (1-\gamma)\left(\sum_{i=1}^{n}\sum_{k=1}^{c} - p_{ik}(q_{ik})\right)$$

Here, x_{ig} represents the normalized expression value of spot i for gene g with $\hat{x}_{ig}$ being the reconstructed value. p_{ik} represents the probability of spot i belonging to cell type k, coded as 1 if spot i is of cell type k, and 0 otherwise. q_{ik} represents the predicted probability, c is the number of cell types, and γ is the hyperparameter that balances the reconstruction loss and cross-entropy loss. In practice, γ is set to 0.5 in most cases. In scenarios where annotated cell types are unavailable, γ is set to 1. Of note, cell type annotations are included to improve embedding accuracy, but they are not strictly necessary, as they can largely be captured by gene expression profiles (Supplementary Fig. 22). During the training process, the Adam optimizer[61] is utilized to minimize the loss function and the exponential linear unit (ELU)[62] is used as the activation function. The weight decay is set to 10^{-4}, and the maximum number of iterations is set to 1,000. The iteration is considered as converged when $|L^{t+1} - L^t| < 10^{-4}$.

Identification of homogeneous spots. The embedding matrix Z integrates information from gene expression values, spatial locations of spots, and cell type priors. We then identify homogeneous spots for each focal spot on the basis of their cosine similarity in this latent space:

$$\cos(\theta_{ij}) = \frac{\mathbf{Z}_i^{\top}\mathbf{Z}_j}{\|\mathbf{Z}_i\|\|\mathbf{Z}_j\|}$$

where $\mathbf{Z}_i \in \mathbb{R}^{m \times 1}$ is the embedding vector of spot i. For each focal spot, we select the top d spots that show the highest cosine similarity with it. This process aligns each individual spot with d spots that are spatially close and share similar transcriptomic profiles, referred to as the microdomain (D). In this study, we set d to 20 for ST data generated from the 10X Visium platform and 50 for ST data generated from the Stereo-seq platform.

Estimation of GSS. We rank genes in individual spots on the basis of their expression levels, with higher expression values receiving higher ranks. We opt to use gene expression ranks instead of gene expression values because the ranks are more robust against artefacts across different technical and biological replicates (Supplementary Fig. 23), as previously suggested[63]. For each gene, its expression specificity within each focal (individual) spot is assessed by calculating the geometric mean of its expression rank across the microdomain of the focal spot, divided by the geometric mean of its expression rank across all spots in the ST data. For gene g, F_{ig} represents its expression specificity in spot i, calculated as:

$$F_{ig} = \frac{\sqrt[d+1]{R_{ig}(\prod_{k \in D_i} R_{kg})}}{\sqrt[n]{\prod_{j=1}^{n} R_{jg}}}$$

where R_{ig} denotes the expression rank of gene g in spot i, and D_i represents the microdomain (that is, set of homogonous spots) of spot i with d denoting the spot number. If $F_{ig} < 0$, indicating that this gene is not specifically expressed within the focal spot, we set it to 0. Additionally, we compare the expression proportion of each gene across the focal spot microdomain to its proportion across all spots. If this ratio is smaller than 1, suggesting that the large F_{ig} might be due to outliers with discordant high expression ranks, we also set F_{ig} to 0. To align the scale between GWAS summary statistics and the estimated gene specificity, we performed an exponential projection to further distinguish genes with high expression specificity:

$$S_{ig} = \exp\{F_{ig}^2\} - 1$$

where S_{ig} denotes the final specificity score of gene g in spot i.

Mapping GSSs to SNPs. We map the specificity score of each gene to the corresponding SNPs within a window extending 50 kb upstream and 50 kb downstream of each gene's transcribed region. We have shown through a sensitive analysis that gsMap is robust to different window sizes (Supplementary Fig. 24). We have included an option in the gsMap software tool for mapping SNPs outside the 100-kb window to genes, based on SNP-to-gene linking maps derived from epigenomic data (for example, Roadmap[15] and Activity-by-Contact model[16]). This process yields a unique set of SNP annotations for each spot. On average, across the ST datasets used in this study, there are more than 150,000 SNPs and 3,000 genes with a non-zero GSS per spot.

Linking genomic annotations with GWAS data. Treating each spot as a set of SNP annotations, gsMap assesses whether SNPs with higher GSS are enriched for heritability for the trait of interest using the S-LDSC[17] framework, conditional on the baseline SNP annotations. The S-LDSC in gsMap can be considered as a linear regression analysis between GWAS χ^2 statistics and stratified LD scores computed using SNP annotations from individual spots. A detailed explanation of S-LDSC can be found in section 2 of the Supplementary Note. The LD reference data used in this study were obtained from the 1000 Genomes Project Phase 3 (1KGP3)[64]. Following previous studies[10,65], we use block-jackknife to estimate the standard error of the regression coefficient in S-LDSC. P value is computed using a one-sided z-test, assessing whether the regression coefficient is significantly larger than 0. A smaller P value indicates a stronger relevance of the focal spot to the trait of interest.

Estimating the strength of enrichment for a spatial region. To evaluate relevance between a specific spatial region and the trait of interest, gsMap uses the Cauchy combination test[19] to aggregate P values of individual spots within the spatial region:

$$T_{\text{Cauchy}} = \sum_{i=1}^{\phi} \tan\{(0.5 - P_i)\pi\}$$

where P_i represents the P value of spot i belonging to the spatial region. The aggregated P value for the spatial region is approximated as:

$$P_{\text{region}} \approx \frac{1}{2} - \pi\{\arctan(T_{\text{Cauchy}})\}$$

The Cauchy combination test combines signals from all spots within a spatial domain, demonstrating high consistency (median $r = 0.82$) with the previous domain-level approach[13] while offering improved statistical power (Supplementary Fig. 21).

Running time. We have optimized the gsMap code to ensure its efficiency in handling large ST data. gsMap analyses large ST datasets with 120 K spots within 3 CPU hours, whereas even with the single-spot GSS available, using S-LDSC software for the same task would require over 20,000 CPU hours (~10 min per spot). A summary of the gsMap runtime for each step is available in section 3 of the Supplementary Note.

Diagnostic tools. We have included a module in the gsMap software tool, which enables users to plot spatial distributions of expression levels and GSS for selected genes, as well as generate Manhattan plots highlighting SNP association signals mapped to these genes, aiding in the diagnostic analysis of the data (Supplementary Fig. 25).

Joint analysis mode. We have developed a joint analysis mode to analyse ST data with multiple technical and/or biological replicates, producing unified results and simplifying interpretation (Supplementary Fig. 26). In brief, a GSS is calculated for each spot as the mean rank of a gene within homogeneous spots, normalized by its mean rank across all spots (including those from different biological replicates). This step harmonizes GSS annotations across biological replicates. We then perform heritability enrichment analysis (for example, using S-LDSC) to associate each spot with traits and apply the Cauchy combination test to combine P values across all spots with the same annotations

Quantifying the association of a spatial region with a trait relative to all other regions

We used an OR, computed as the ratio of trait-associated spots to non-associated ones in a specific region divided by the ratio in all other regions, to compare gsMap results of a specific spatial region across traits with varied GWAS statistical power. This metric quantifies the strength of a region's association with a trait, relative to all other regions. Consequently, it compensates for differences in gsMap results owing to variations in GWAS statistical power, allowing for a more meaningful comparison of gsMap results across traits. The significance of the OR was evaluated using a Chi-square test.

Simulations

The simulation study was conducted using real genotype data on 100,000 unrelated individuals of European ancestry from the UK Biobank[22]. We used the HapMap3 SNPs and filtered out SNPs with a minor allele frequency (MAF) < 0.01 or Hardy–Weinberg equilibrium test P value < 10^{-6}, resulting in a total of 1,195,548 SNPs. We used GCTA (V1.94.1)[66] to generate quantitative traits based on real genotype data of a set of selected causal variants. We simulated four null scenarios where causal variants were: (1) randomly distributed across the genome; (2) enriched in the candidate *cis*-regulatory elements (cCREs)[67]; (3) enriched within LD blocks; and (4) enriched in the *cis*-regions of non-spatially variable genes (NSVGs), respectively. Here 'null' means that the simulated causal variants are not enriched in or around genes with context-dependent expression, meaning that the simulated trait is not expected to be associated with any specific group of spots.

In scenario 1, we simulated phenotypes with varying levels of polygenicity (that is, proportion of SNPs being causal) and heritability (that is, proportion of variance in the phenotype attributed to the causal SNPs). The number of causal SNPs varied from 10,000 to 500,000, and the heritability ranged from 0.1 to 0.6. In scenarios 2 to 4, we fixed the number of causal SNPs at 100,000 and heritability at 0.3. For scenario 4, we used two strategies to select NSVGs. First, we chose genes with a maximum GSS smaller than 1.5, computed by gsMap. Second, to select genes entirely independent of the gsMap analysis process, we used SPARK-X[68] to test for spatially dependent expression and selected genes with a P value greater than 0.85. Each simulation was replicated three times. We used PLINK (V1.90)[69] to associate SNPs with the simulated phenotypes with the first ten principal components, derived from SNPs, fitted as covariates.

GWAS summary statistics

We collected GWAS summary statistics from the public domain for a broad range of complex traits and diseases, spanning eight major categories: autoimmune, psychiatric, reproductive, behavioural, metabolic, haematological, anthropometric and cancer. To ensure sufficient GWAS power, we included only those traits for which the Chi-square statistic for the LDSC estimate of heritability exceeded 25, as suggested by prior work[8,10]. In summary, we analysed GWAS summary statistics for 110 complex traits, including diseases, from the UK Biobank and other publicly available sources (average n = 385,000, Supplementary Table 1). We excluded the major histocompatibility complex (MHC) region from all analyses owing to its complexity[17].

Spatial transcriptomics datasets

We included six spatial transcriptomics datasets in this study: mouse embryonic data (Stereo-seq)[5], human embryonic data (Stereo-seq)[7], mouse brain data (Stereo-seq and MERFISH)[5,27], macaque cortical data (Stereo-seq) and human DLPFC data (10X Visium)[13]. To align mouse or macaque genes with human genes, we utilized the biomaRt (V3.18) R package to conduct homologous gene transformations. The average gene numbers after homologous transformation are 16,330 for the mouse datasets and 13,536 for the macaque dataset. Following the standard analysis pipeline, we utilized the Scanpy (V1.9.6)[59] Python package to process each ST dataset. Details of each dataset are summarized below.

Mouse embryonic ST data. We analysed 54 coronal sections from the mouse embryonic dataset, sourced from eight C57BL/6J mice, with an average of 81,125 spots per section, spanning from the embryonic stage of E9.5 to E16.5[5]. Data at both bin50 resolution (53 sections) and single-cell resolution (1 section) were included in this study. We obtained access to the h5ad files, each including the gene expression count matrix, cell type annotations, and spot spatial coordinates for a section. We validated the cell type annotations based on known marker genes.

Human embryonic ST data. We analysed 62 transverse sections from the human embryonic dataset, sourced from a CS8 human embryo of Chinese ancestry, with a total of 38,562 spots[7]. We had access to the h5ad files, each containing the gene expression count matrix, cell type annotations, and spot spatial coordinates.

Mouse brain ST data. We analysed two sections from the mouse brain dataset: one coronal section from an adult C57BL/6J mouse brain (50,140 spots) and one sagittal section from an E16.5 embryonic C57BL/6J mouse brain (65,303 spots)[5]. Both sections are at single-cell resolution. We had access to the h5ad files and verified the cell type annotations using known marker genes.

Mouse brain MERFISH ST data. We analysed a mouse brain MERFISH ST dataset[27] consisting of two sections: a coronal section from an adult C57BL/6J-1 mouse brain containing 41,181 spots and a sagittal section from an adult C57BL/6J-3 mouse brain containing 105,934 spots. This dataset was generated using an image-based platform, where a panel of ~1,100 genes was imaged. The remaining genes were imputed by the authors using paired scRNA-seq data. We accessed the imputed ST dataset, which includes expression levels for 15,768 genes, cell spatial coordinates, cell type annotations, and brain region annotations.

Macaque cortical ST data. We analysed 162 coronal sections from the macaque cerebral cortical dataset, sourced from three adult male cynomolgus monkeys, with an average of 266,654 spots per section[35]. All sections are at single-cell resolution. We obtained access to the sctransform[70] gene expression matrices and the metadata files. For each section, we aligned the spots spatial coordinates, cell type annotations, cortical region annotations, and section-cutting positions (EBZ) and compiled all the aforementioned information into an h5ad file.

Human DLPFC ST data. We analysed eight coronal sections from the adult human DLPFC dataset, sourced from two donors of European ancestry, with an average of 3,973 spots per section[13]. These data were generated using 10X Visium, with each spot containing a few dozen cells. We had access to the h5ad files, each including the gene expression count matrix, spots spatial coordinates, and cortex layer annotations.

Single-cell RNA-seq datasets

We used six scRNA-seq datasets in this study to estimate gene expression correlations between mice and humans[47,71–75]. These datasets contain 9 million cells, covering 25 major tissues from both mice and humans. The cell type annotations were provided by the authors of the scRNA-seq datasets, and we re-clustered them into eight primary cell categories: endothelial cells, epithelial cells, glial cells, neurons, immune cells, muscle cells, stem cells and others.

Comparison of the gsMap results from the human and macaque datasets

We applied gsMap to eight human DPLFC ST sections and observed highly consistent results across these sections. We then calculated an OR for each cortex layer, representing the strength of association of a cortex layer with a trait, relative to all other layers. To ensure a robust comparison between the human and macaque results, we compared the median OR value of each cortex layer across eight human DPLFC ST sections to that across nine macaque PFC ST sections. Considering that there were only five matched cortex layers between the human and macaque datasets, we pooled the OR values from 22 brain-related traits, resulting in 110 data points in the comparison analysis.

Integration of GWAS summary statistics with ST data using scDRS

scDRS[9] is a method that can integrate GWAS summary statistics with scRNA-seq data to identify cells relevant to a trait. In brief, scDRS computes a trait-enrichment score to examine whether a cell has excess expression levels across a set of trait-associated genes. These genes were derived from GWAS summary statistics using gene-based association tests (for example, MAGMA[76]). To assess the statistical significance of the trait-enrichment score, a P value is calculated by comparing the trait-enrichment score to those computed from control genes with matched expression characteristics. Though originally developed for scRNA-seq data, scDRS can, in principle, be applied to ST data by regarding each spot in the ST data as a cell. Following the standard analysis protocol of scDRS (V1.03), we first used MAGMA to generate gene-based test statistics from the GWAS summary statistics, utilizing reference LD data obtained from 1KGP3, as done in gsMap analysis. Next, we used the 'munge-gs' command in scDRS and set the 'n-max' parameter to 1,000, to generate a gene-weight file for the top 1000 trait-associated genes identified from the MAGMA analysis. Finally, we used the 'compute-score' command in scDRS and set the 'n-ctrl' parameter to 1,000, which generated 1,000 sets of control genes using Monte Carlo sampling, to obtain the trait-enrichment P value for each spot.

Expression association analysis

We performed two expression association analyses to identify genes whose expression levels in Glu-neurons were associated with their positions along the CA1 D–V axis, and genes in Glu-neurons whose expression levels were associated with their relevance to SCZ.

Expression association analysis-1 (for gene g):

$$\mathbf{g} = \mathbf{x}\beta + \mathbf{c}\alpha + e$$

where $\mathbf{g} \in \mathbb{R}^{k\times 1}$ represents the normalized expression levels of a gene in k Glu-neurons, $\mathbf{x} \in \mathbb{R}^{k\times 1}$ represents the spatial positions of k

Glu-neurons along the D–V axis, with β being the coefficients, $\mathbf{c} \in \mathbb{R}^{k\times 1}$ represents the spot library size vector (a sum of all UMI counts per spot) to adjust for the gene expression variation attributed to spot library size, and e represents the residuals.

Expression association analysis-2 (for gene g):

$$\mathbf{g} = \mathbf{z}\gamma + \mathbf{c}\alpha + e$$

where $\mathbf{z} \in \mathbb{R}^{k\times 1}$ represents the $-\log_{10}$ gsMap P values of associations between k Glu-neurons and a trait of interest (for example, SCZ), with γ being the coefficients. The other parameters are defined as above.

Gene prioritization for complex traits

We compared the genes prioritized by gsMap to those identified by other gene prioritization methods, including COLOC[77], FUSION[78], SMR[79] and PoPS[80] for the psychiatric disorders (including depression, bipolar disorder and schizophrenia) for which a number of drug target genes are available for validation. We used all eQTL datasets from GTEx[81] for FUSION (V1.0.0), all eQTL datasets from GTEx[81] and MetaBrain[82] for COLOC (V5.2.3) and SMR (V1.3.1), and the feature matrix provided by the PoPS authors for PoPS (V0.2).

Psychiatric drug targets

We collected drug target genes from the DrugBank database[43] and Drug Repurposing Hub database[42]. For the DrugBank database, we selected drugs intended to treat psychiatric disorders categorized under the International Classification of Diseases (ICD) codes F00 to F99. From the Drug Repurposing Hub database, we selected drugs categorized under the psychiatric disease areas. In total, we identified 417 target genes from drugs that are either approved or undergoing clinical trials for treating psychiatric disorders. Based on the identified drug target genes, we used Fisher's exact test to assess whether genes highly expressed in the macaque PFC 14r region are enriched in these drug target genes, compared to all detected genes, or genes highly expressed in other PFC regions. The module score of these 417 drug targets genes for individual spots was computed using the AddModuleScore function in the Seurat (V4.4.0) R package with the default settings[83,84]

GO term enrichment

We performed GO term enrichment analysis using the clusterProfiler[85] (V3.18) R package with the default settings.

Genetic correlation

We used the bivariate LDSC[65,86] (V1.01) to estimate genetic correlations between trait pairs. The reference LD data used in the genetic correlation analysis was generated from 1KGP3.

Statistics and reproducibility

We analysed only existing datasets without using any statistical methods to predefine the sample size. Our study did not involve a design requiring randomization or blinding. We validated our results by performing the same analyses on independent datasets, and all replication analyses were successful.

Reporting summary

Further information on research design is available in the Nature Portfolio Reporting Summary linked to this article.

Data availability

This study used GWAS summary statistics for 110 traits, as summarized in Supplementary Table 1. The mouse embryonic and brain ST data are available at China National GeneBank DataBase (CNGBdb) under accession CNP0001543. The human embryonic ST data are available at The National Genomics Data Center (NGDC) Genome Sequence Archive (GSA) under accession HRA005567. The mouse brain MERFISH ST data are available at https://cellxgene.cziscience.com/collections/0cca8620-8dee-45d0-aef5-23f032a5cf09. The macaque cortical ST data are available at CNGBdb under accession CNP0002035. The human DLPFC ST data are available at https://research.libd.org/globus/. The scRNA-seq data from human and mouse are available at: https://cellxgene.cziscience.com/. The reference LD data, generated from 1KGP3, are available at ftp://ftp.1000genomes.ebi.ac.uk/vol1/ftp/release/2013050. The LDSC baseline functional annotations are available at https://data.broadinstitute.org/alkesgroup/LDSCORE. The DrugBank database is available at https://go.drugbank.com/releases/latest. The Drug Repurposing Hub database (version of 24 March 2020) is available at https://repo-hub.broadinstitute.org/repurposing#download-data. The human, mouse, and macaque reference genome data are available at https://nov2020.archive.ensembl.org/index.html. The gsMap results for different traits and ST datasets can be visualized and downloaded at https://yanglab.westlake.edu.cn/gsmap/home. Source data are provided with this paper.

Code availability

The source code for gsMap is available on GitHub (https://github.com/JianYang-Lab/gsMap) and Zenodo (https://doi.org/10.5281/zenodo.14744887 (ref. 87)).

55. Du, J. et al. Advances in spatial transcriptomics and related data analysis strategies. *J. Transl. Med.* **21**, 330 (2023).
56. Hu, J. et al. SpaGCN: Integrating gene expression, spatial location and histology to identify spatial domains and spatially variable genes by graph convolutional network. *Nat. Methods* **18**, 1342–1351 (2021).
57. Yuan, Z. et al. Benchmarking spatial clustering methods with spatially resolved transcriptomics data. *Nat. Methods* **21**, 712–722 (2024).
58. Vicar, T. et al. Cell segmentation methods for label-free contrast microscopy: review and comprehensive comparison. *BMC Bioinformatics* **20**, 360 (2019).
59. Wolf, F. A., Angerer, P. & Theis, F. J. SCANPY: large-scale single-cell gene expression data analysis. *Genome Biol.* **19**, 15 (2018).
60. Veličković, P. et al. Graph attention networks. In *International Conference on Learning Representations (ICLR)* (ICLR, 2018).
61. Kingma, D. P. & Ba, J. Adam: a method for stochastic optimization. In *International Conference on Learning Representations (ICLR)* (ICLR, 2015).
62. Clevert, D.-A., Unterthiner, T. & Hochreiter, S. Fast and accurate deep network learning by exponential linear units (ELUs). In *International Conference on Learning Representations (ICLR)* (ICLR, 2016).
63. Theodoris, C. V. et al. Transfer learning enables predictions in network biology. *Nature* **618**, 616–624 (2023).
64. Auton, A. et al. A global reference for human genetic variation. *Nature* **526**, 68–74 (2015).
65. Bulik-Sullivan, B. K. et al. LD Score regression distinguishes confounding from polygenicity in genome-wide association studies. *Nat. Genet.* **47**, 291–295 (2015).
66. Yang, J., Lee, S. H., Goddard, M. E. & Visscher, P. M. GCTA: a tool for genome-wide complex trait analysis. *Am. J. Hum. Genet.* **88**, 76–82 (2011).
67. Abascal, F. et al. Expanded encyclopaedias of DNA elements in the human and mouse genomes. *Nature* **583**, 699–710 (2020).
68. Zhu, J., Sun, S. & Zhou, X. SPARK-X: non-parametric modeling enables scalable and robust detection of spatial expression patterns for large spatial transcriptomic studies. *Genome Biol.* **22**, 184 (2021).
69. Chang, C. C. et al. Second-generation PLINK: rising to the challenge of larger and richer datasets. *Gigascience* **4**, 7 (2015).
70. Hafemeister, C. & Satija, R. Normalization and variance stabilization of single-cell RNA-seq data using regularized negative binomial regression. *Genome Biol.* **20**, 296 (2019).
71. Siletti, K. et al. Transcriptomic diversity of cell types across the adult human brain. *Science* **382**, eadd7046 (2023).
72. The Tabula Sapiens Consortium The Tabula Sapiens: a multiple-organ, single-cell transcriptomic atlas of humans. *Science* **376**, eabl4896 (2022).
73. Cao, J. et al. A human cell atlas of fetal gene expression. *Science* **370**, eaba7721 (2020).
74. Almanzar, N. et al. A single-cell transcriptomic atlas characterizes ageing tissues in the mouse. *Nature* **583**, 590–595 (2020).
75. Qiu, C. et al. A single-cell time-lapse of mouse prenatal development from gastrula to birth. *Nature* **626**, 1084–1093 (2024).
76. de Leeuw, C. A., Mooij, J. M., Heskes, T. & Posthuma, D. MAGMA: generalized gene-set analysis of GWAS data. *PLoS Comput. Biol.* **11**, e1004219 (2015).
77. Giambartolomei, C. et al. Bayesian Test for Colocalisation between Pairs of Genetic Association Studies Using Summary Statistics. *PLoS Genet.* **10**, e1004383 (2014).
78. Gusev, A. et al. Integrative approaches for large-scale transcriptome-wide association studies. *Nat. Genet.* **48**, 245–252 (2016).
79. Zhu, Z. et al. Integration of summary data from GWAS and eQTL studies predicts complex trait gene targets. *Nat. Genet.* **48**, 481–487 (2016).
80. Weeks, E. M. et al. Leveraging polygenic enrichments of gene features to predict genes underlying complex traits and diseases. *Nat. Genet.* **55**, 1267–1276 (2023).

81. The GTEx Consortium The GTEx Consortium atlas of genetic regulatory effects across human tissues. *Science* **369**, 1318–1330 (2020).
82. de Klein, N. et al. Brain expression quantitative trait locus and network analyses reveal downstream effects and putative drivers for brain-related diseases. *Nat. Genet.* **55**, 377–388 (2023).
83. Stuart, T. et al. Comprehensive integration of single-cell data. *Cell* **177**, 1888–1902.e1821 (2019).
84. Tirosh, I. et al. Dissecting the multicellular ecosystem of metastatic melanoma by single-cell RNA-seq. *Science* **352**, 189–196 (2016).
85. Yu, G., Wang, L. G., Han, Y. & He, Q. Y. clusterProfiler: an R package for comparing biological themes among gene clusters. *Omics* **16**, 284–287 (2012).
86. Bulik-Sullivan, B. et al. An atlas of genetic correlations across human diseases and traits. *Nat. Genet.* **47**, 1236–1241 (2015).
87. Liyang, S., Wenhao, C., Junren, H., Minmin, G. & Jian, Y. Spatially resolved mapping of cells associated with human complex traits. *Zenodo* https://doi.org/10.5281/zenodo.14744887 (2025).

Acknowledgements The authors thank B. Li and Q. Ma for their insightful suggestions in interpreting the results from the brain-related analyses; and F. Cheng, S. Liu, G. Dong, S. Sun, L. Li and Y. Guo for their valuable discussions and assistance in writing the manuscript; the Westlake University High-Performance Computing Center for their assistance in computing; and all the authors who have made the GWAS, ST and scRNA-seq data publicly accessible.

This research was supported by the National Natural Science Foundation of China (U23A20165), the Leading Innovative and Entrepreneur Team Introduction Program of Zhejiang (2021R01013), 'Pioneer' and 'Leading Goose' R&D Program of Zhejiang (2022SDXHDX0001 and 2024SSYS0032), and the Westlake University Research Center for industries of the Future (WU2022C002 and WU2023C010).

Author contributions J.Y. and L.S. conceived the study and designed the experiment. L.S. developed the methods with input from W.C. and J.Y. L.S. and W.C. developed the software tool. L.S. and W.C. curated the data and conducted all analyses under the guidance of J.Y. J.H. and M.G. developed the interactive website. J.Y. supervised the project. L.S. and J.Y. wrote the manuscript with the participation of W.C. All authors reviewed and approved the final manuscript.

Competing interests The authors declare no competing interests.

Additional information

Supplementary information The online version contains supplementary material available at https://doi.org/10.1038/s41586-025-08757-x.

Correspondence and requests for materials should be addressed to Jian Yang.

Peer review information *Nature* thanks J. Baillie, Nilanjan Chetterjee, Andrew Jaffe and the other, anonymous, reviewer(s) for their contribution to the peer review of this work. Peer review reports are available.

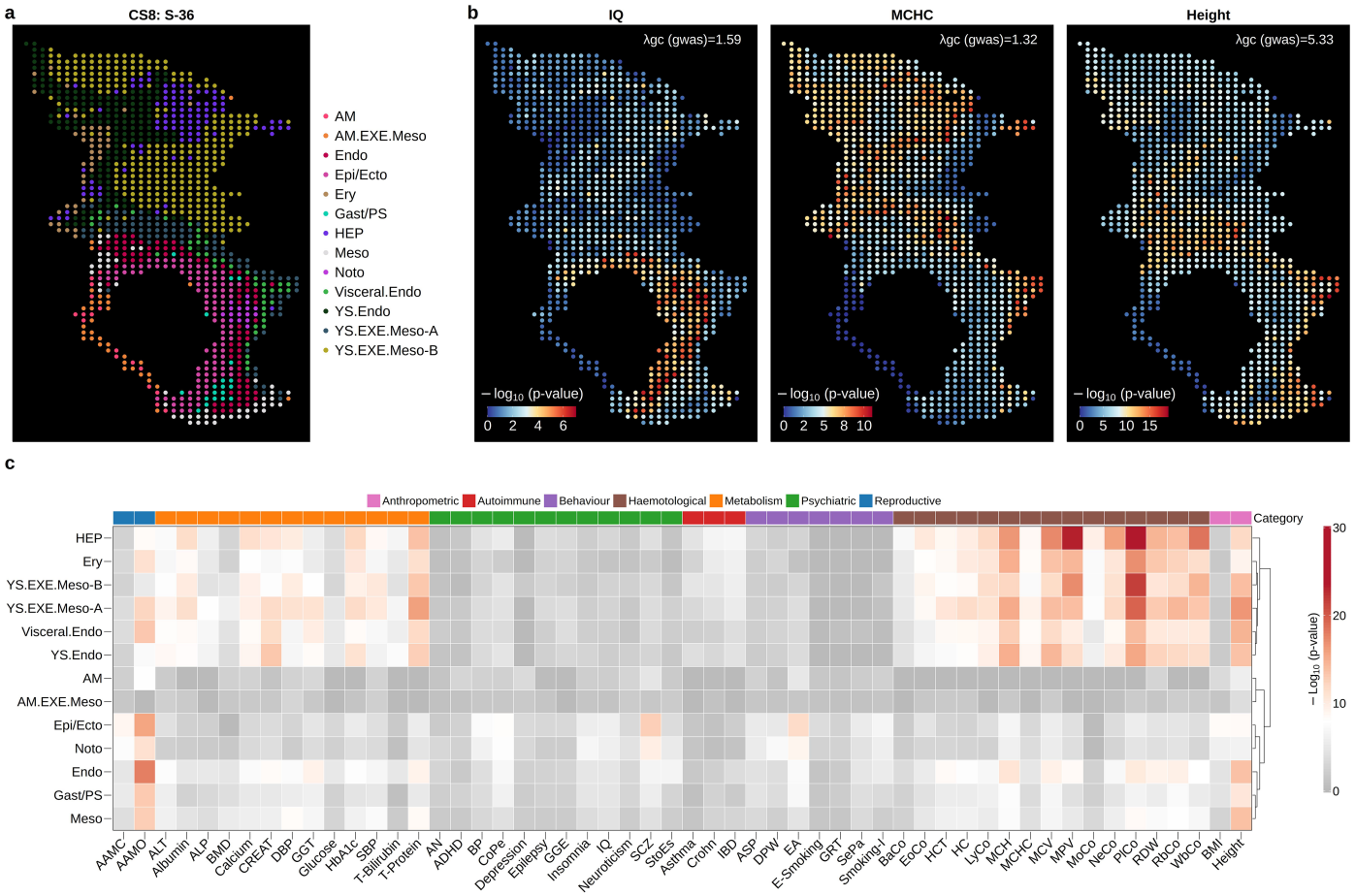

Extended Data Fig. 1 | Mapping human complex traits to human embryo. a) Human CS8 embryonic ST data[7], with spots colored by their tissue types. b) gsMap results for IQ, MCHC, and height using the human CS8 embryonic ST data, with colors indicating the significance of spot-trait associations. The genomic inflation, λ_{GC}, serves as an indicator of the GWAS statistical power. c) Tissue-trait associations, with colors indicating the significance of the associations and the colored annotations on the right indicating tissue types. Rows correspond to tissue types, and columns represent traits.

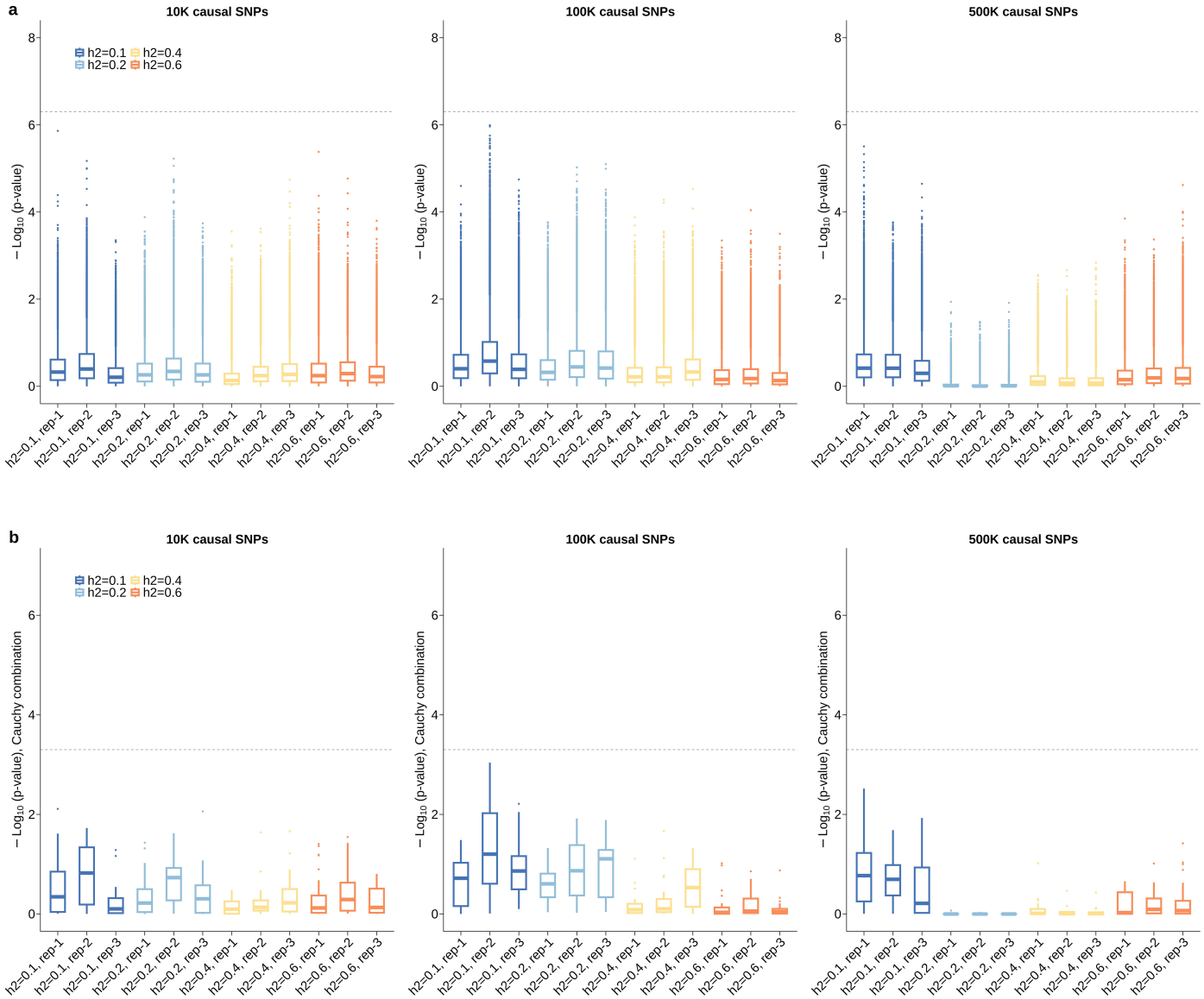

Extended Data Fig. 2 | gsMap results in null simulations where causal variants were randomly distributed across the genome. a-b) Boxplot of gsMap results at the spot level (a, $n = 121{,}767$) and region level (b, $n = 25$) in null simulations with the number of causal SNPs set to 10 K, 100 K, and 500 K. The x-axis displays trait heritability, varying from 0.1 to 0.6, and the y-axis shows the association −log10 *P* value. In each box, the central line denotes the median, notches represent the 95% CI, the box indicates the IQR, and whiskers extend up to 1.5 times the IQR, with outliers shown as individual dots. The dashed line represents the threshold at FDR = 0.05.

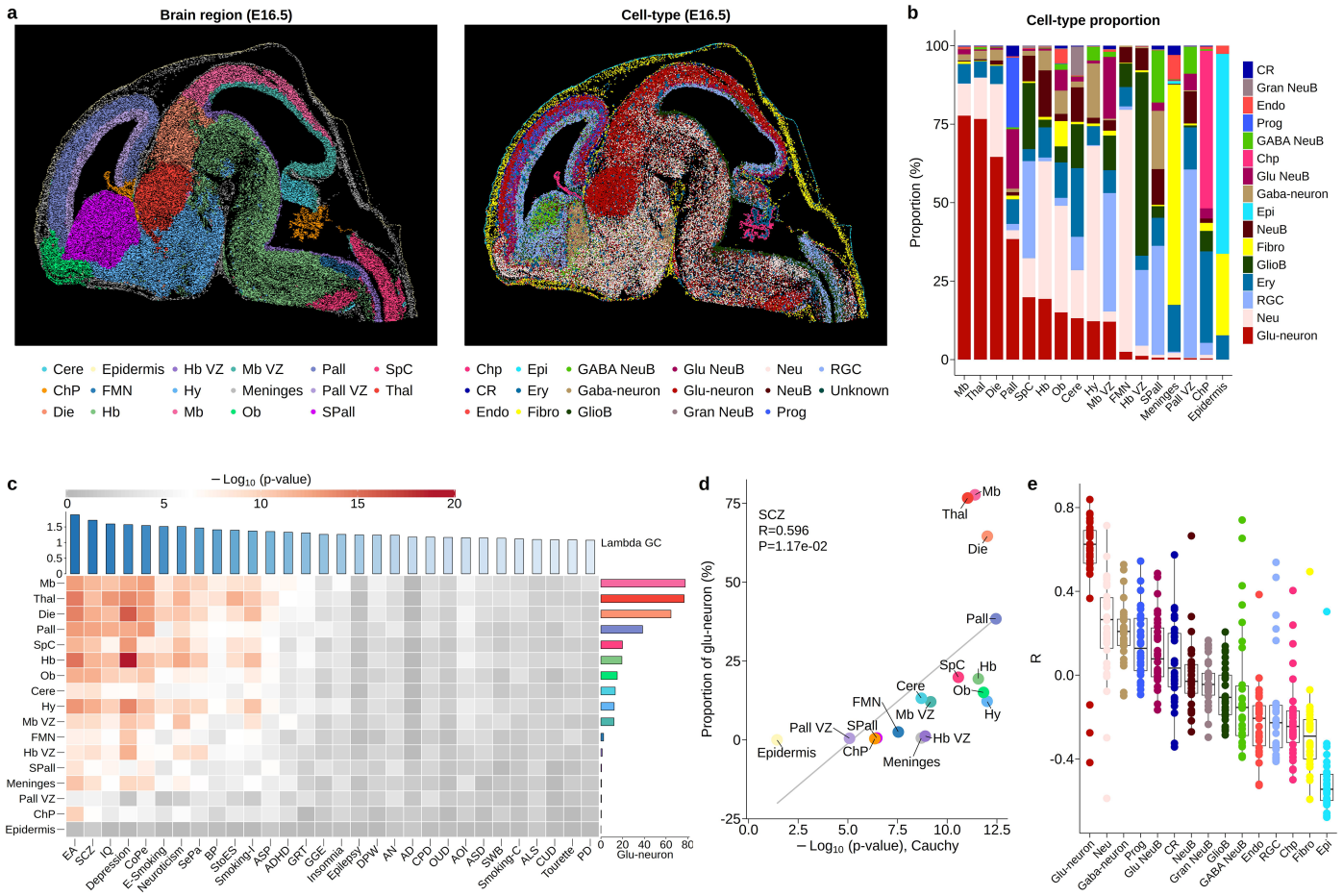

Extended Data Fig. 3 | Mapping human complex traits to embryonic mouse brain. a) Mouse E16.5 embryonic brain ST data, with spots colored by brain regions (Left) or cell types (Right). Abbreviations for brain region and cell types are listed in section 5 of the Supplementary Note. b) Cell type proportions in each brain region. c) Associations of brain regions with different traits, with colors indicating the association significance. Rows represent brain regions, and column represent traits. The colored bar on the right representing the proportion of glu-neurons in each brain region, while the colored bar on the top represents the genomic inflation, λ_{GC}, which serves as an indicator of the statistical power of the GWAS data. d) Correlation between the significance of a brain region's association with SCZ (x-axis) and its proportion of glu-neurons (y-axis). The grey line represents the regression line, with the p-value from a two-sided t-test ($n = 17$). e) Correlation between significance of association with a trait and proportion of a cell type across brain regions. The x-axis displays different cell types; the y-axis shows the correlation coefficient. Point represent traits ($n = 30$), colored by cell types. In each box, the central line denotes the median, notches represent the 95% CI, the box indicates the IQR, and whiskers extend up to 1.5 times the IQR, with outliers shown as individual dots.

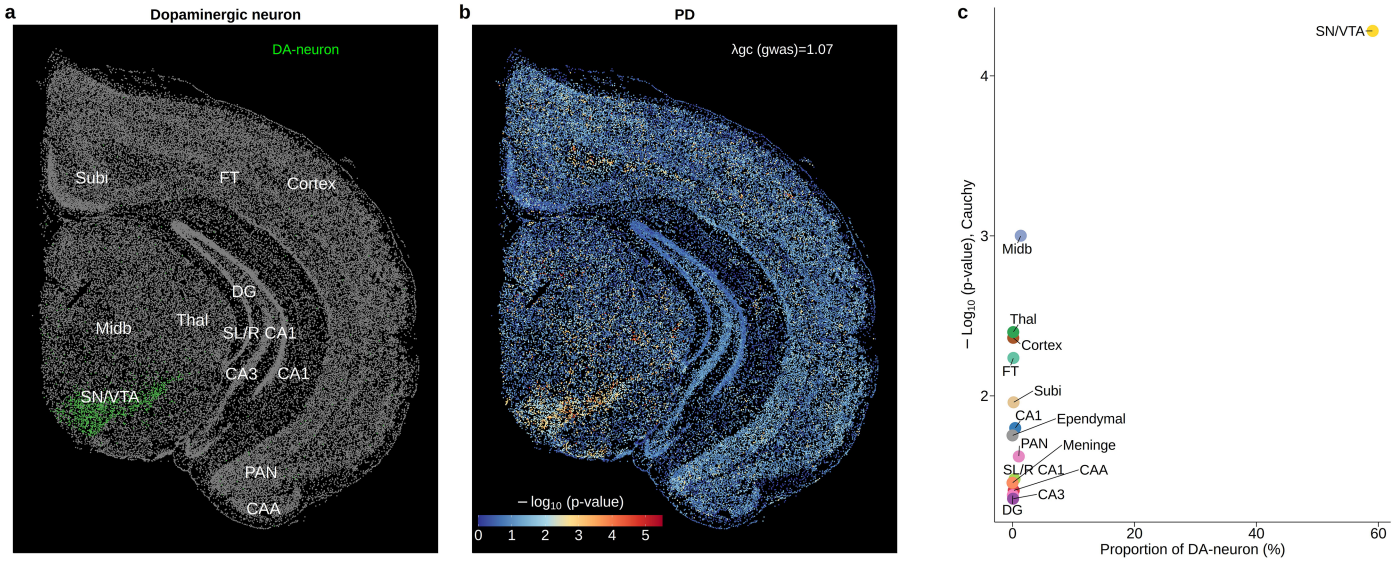

Extended Data Fig. 4 | Mapping Parkinson's Disease to adult mouse brain. a) The distribution of dopaminergic neurons (DA-neurons) on the adult mouse brain ST data, where green points denote DA-neurons. Abbreviations for brain region and cell types are listed in section 5 of the Supplementary Note. b) gsMap results for Parkinson's Disease (PD), where points represent an individual cells colored by the association significance. c) Proportions of DA-neurons in different brain regions (x-axis) and the significance of their associations with PD (y-axis).

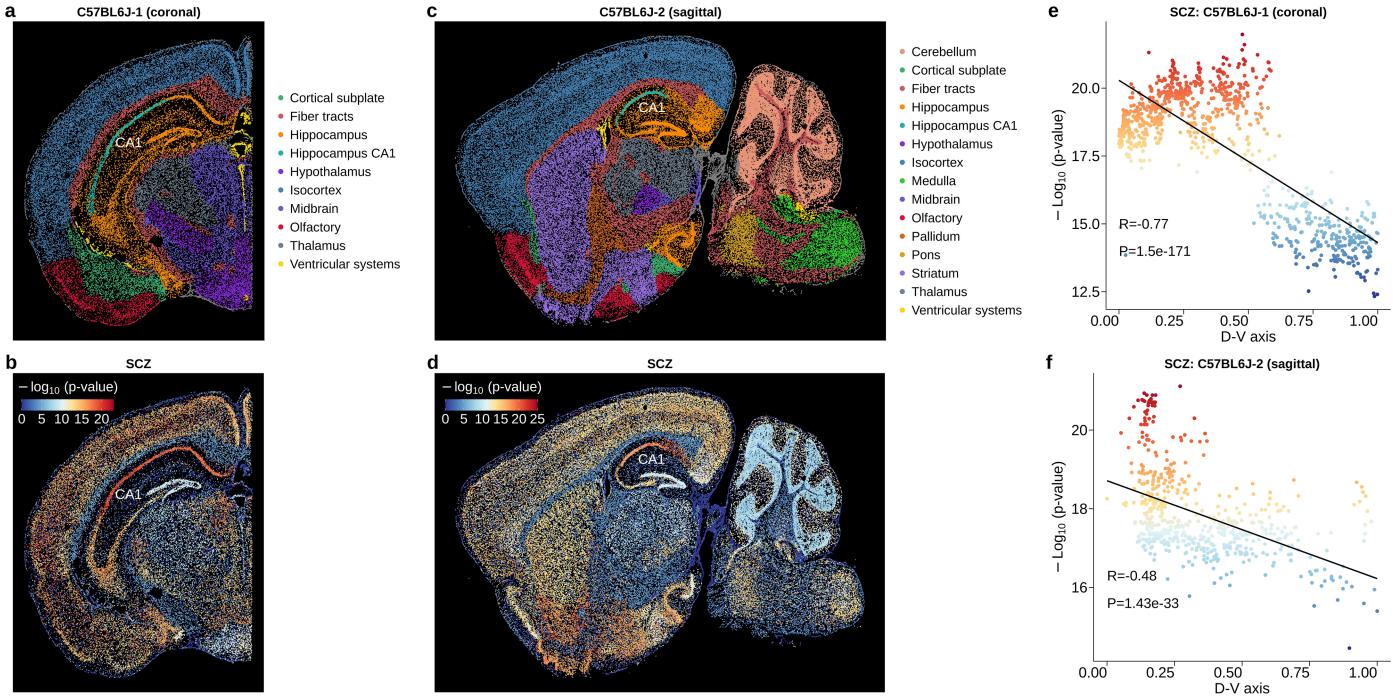

Extended Data Fig. 5 | Spatially dependent associations of CA1 glu-neurons with SCZ using mouse brain MERFISH ST datasets. a) MERFISH ST data of the mouse brain coronal section from mouse individual #1. Points represent individual cells, colored by brain regions. b) gsMap results for SCZ using the mouse brain coronal ST section. c) MERFISH ST data of the mouse brain sagittal section from mouse individual #2. Points represent individual cells, colored by brain regions. d) gsMap results for SCZ using the mouse brain sagittal ST section. e-f) Correlation between the significance of a glu-neuron's association with SCZ and its spatial position along the CA1 D-V axis, using mouse brain coronal (e, $n = 883$) and sagittal ST data (f, $n = 556$). The black lines represent the regression line, with p-values from a two-sided t-test.

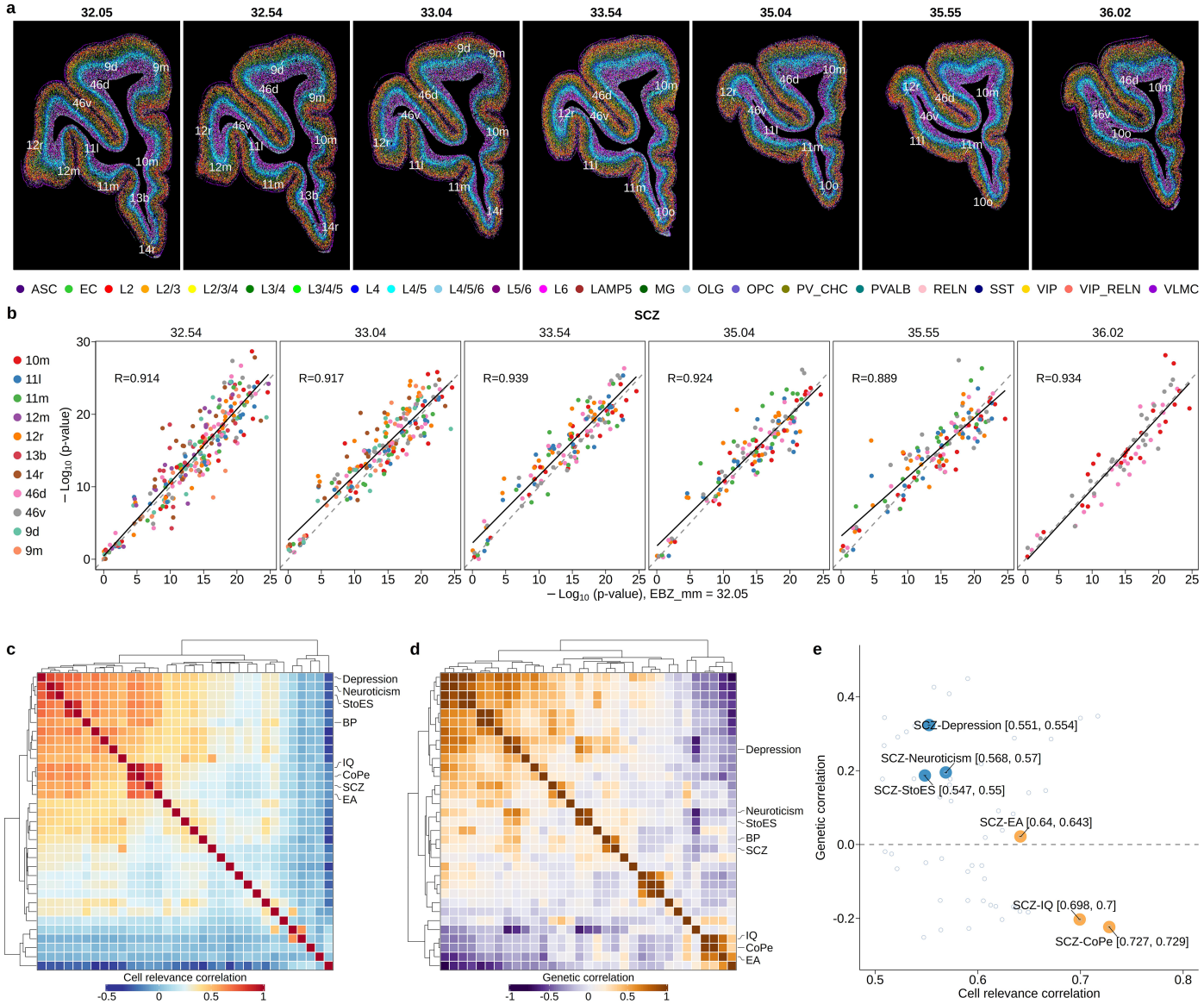

Extended Data Fig. 6 | Mapping human complex traits to adult macaque cerebral cortex. a) Representative ST sections from the left prefrontal cortex of an adult macaque8, with cells colored by cell types. The title of each image displays the cutting position of each ST section, ranging from ear bar zero (EBZ, mm) 32.05 to 36.02. The white texts on the image label cortical regions. b) Cell type-SCZ associations in each of the cortical region estimated using the EBZ 32.05 ST section vs. those estimated using the other ST sections. In each cortical region, we aggregated the individual cells' associations with SCZ into the association of each cell type using the Cauchy combination test. We next calculated the Pearson correlation of -log10(p-values) between ST sections across different cell types and cortical regions. The x-axis displays the associations of cell types with SCZ estimated using the EBZ 32.05 ST section; the y-axis shows the corresponding associations estimated using the ST sections from EBZ 32.54 to EBZ 36.02. Points represent cell types, colored by cortical regions. The black line is the regression line, and the grey dashed line represents the line of equality. c) CRC between traits estimated using gsMap with the macaque cortical ST data. d) Genetic correlations between traits estimated using the bivariate LDSC method. Each column or row represent a trait. e) Scatter plot showing the CRC between traits (x-axis), and the corresponding genetic correlations (y-axis). The orange and blue points highlight the CRC between SCZ and cognitive traits, and mood traits, respectively. The texts in square brackets show the 95% CI of CRC.

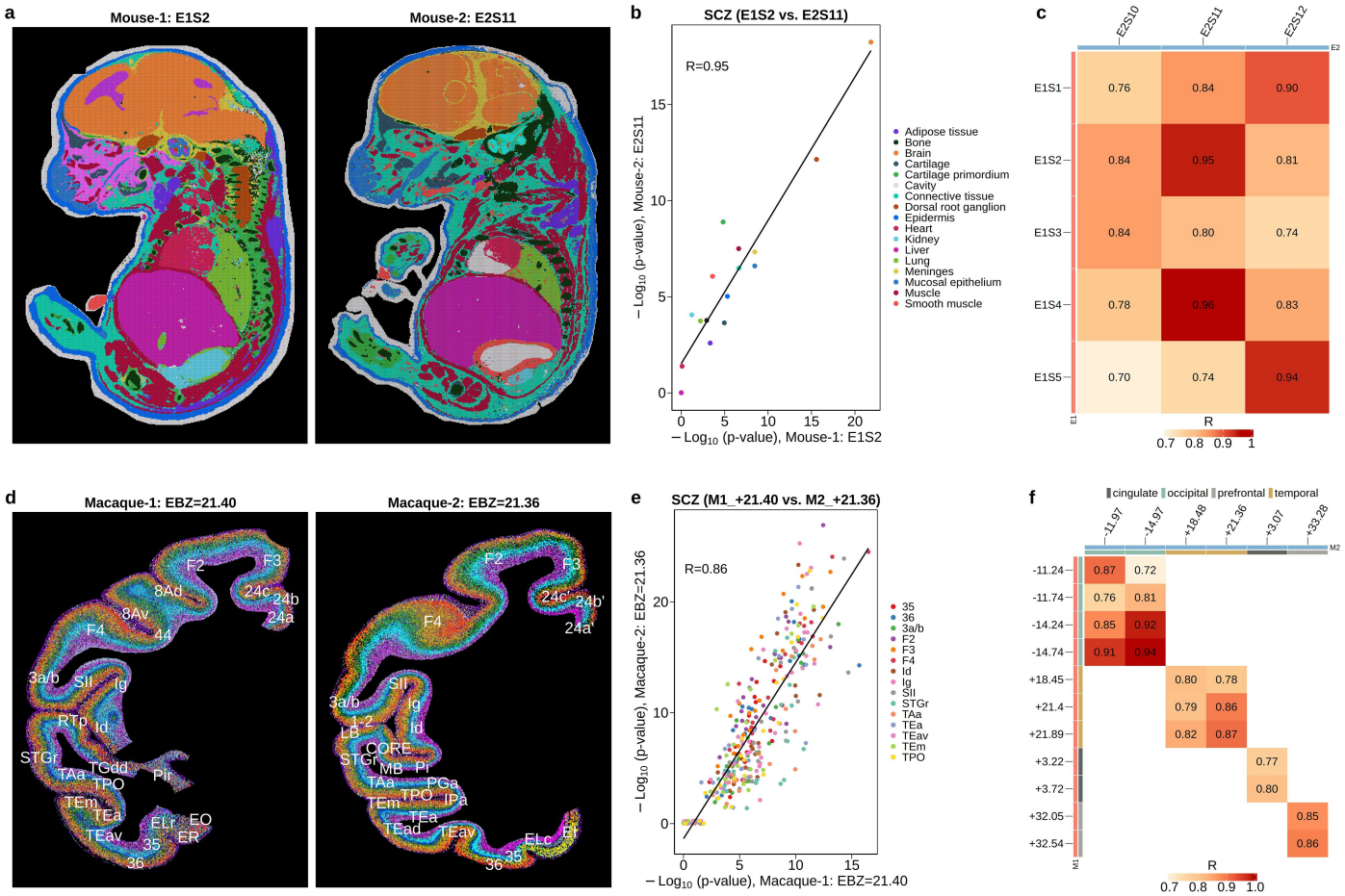

Extended Data Fig. 7 | Correlation of gsMap results among biological replicates. a) Spatially matched embryonic ST sections from mouse individuals #1 and #2, with spots colored by tissue type. b) Tissue-SCZ associations, comparing the E1S2 section from mouse individual #1 (x-axis) with the E2S11 section from mouse individual #2 (y-axis). c) Correlation heatmap of gsMap results for SCZ across 15 pairs of biological replicates, with the x-axis representing embryonic ST sections from mouse individual #1 and the y-axis representing those from mouse individual #2. d) Spatially matched cortical ST sections from macaque individuals #1 and #2, with spots colored by cell type and the cortical regions annotated by text. These sections are from different macaque individuals but were taken at approximately the same cutting positions, calibrated by their distance from the ear bar zero (EBZ). e) Cell type-SCZ associations in each cortical region, comparing the EBZ 21.40 ST section from macaque individual #1 (x-axis) with the EBZ 21.36 ST section from macaque individual #2 (y-axis). f) Correlation heatmap of gsMap results for SCZ across 18 pairs of macaque biological replicates. The x-axis represents ST sections from macaque individual #1, and the y-axis represents those from macaque individual #2. Shown are results from spatially matched ST sections, where the absolute differences in EBZ are smaller than 5 mm and there are more than 10 matched cortical regions.

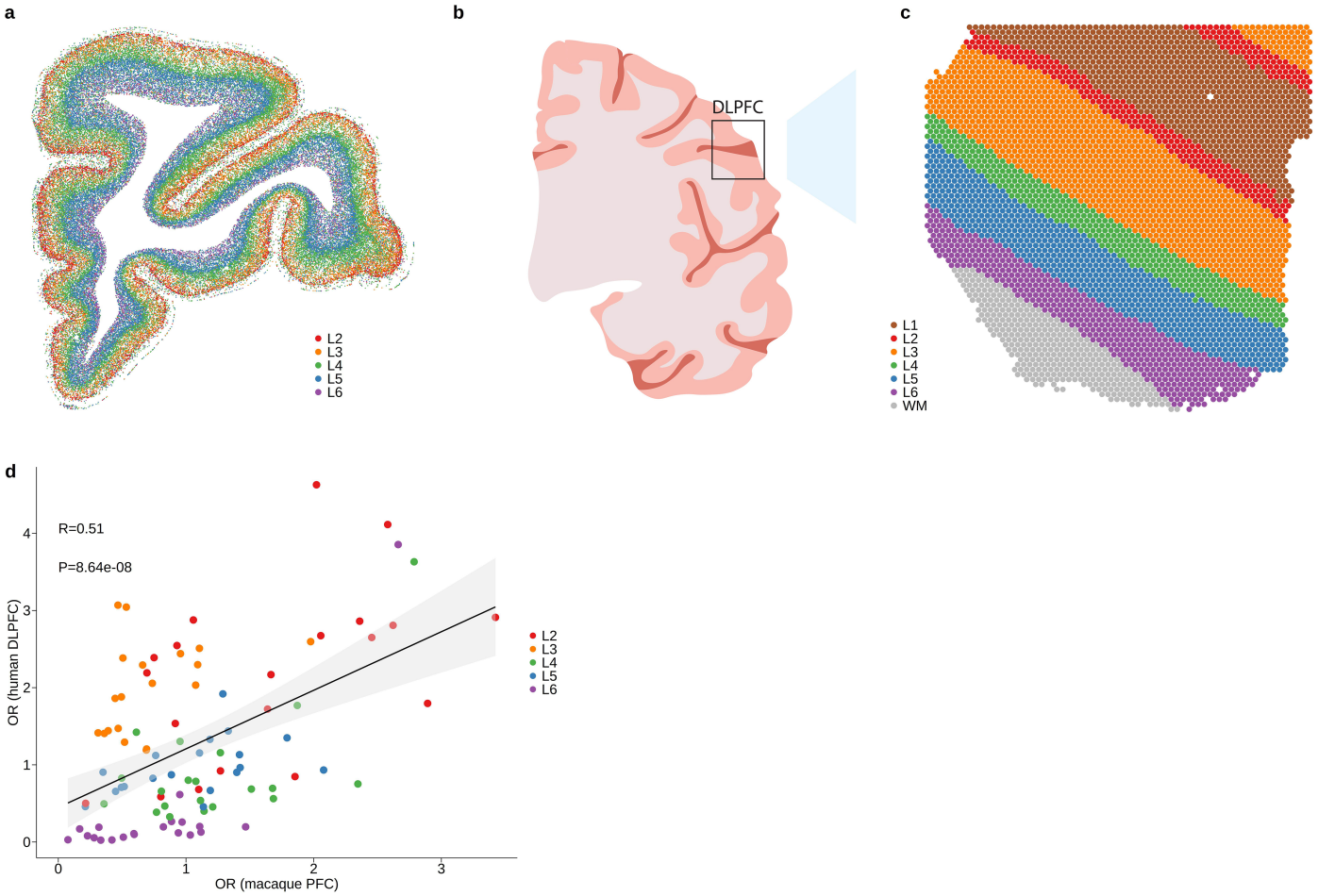

Extended Data Fig. 8 | Comparison of gsMap results between human and macaque. a) Macaque prefrontal cortex (PFC) ST data. Points represent individual cells, with colored by cortex layers. b) Schematic of the PFC and DLPFC. c) Human DLPFC ST data generated by the 10X Visium platform. Points represent individual spots (a few dozen cells), colored by cortex layers. d) Correlation between ORs of cortex layers estimated from the macaque PFC ST data and those estimated from the human DLPFC ST data. To ensure a robust comparison between human and macaque results, we compared the median OR of each cortex layer across 8 human DLPFC ST sections (y-axis) to that across 9 macaque PFC ST sections (x-axis). Considering that there were only 5 matched cortex layers between the human and macaque datasets, we pooled ORs from 22 brain-related traits. Each data point represents the OR of a cortex layer for a trait. The center black line is the regression line, with the shaded area indicating the 95% CI. The p-value is from a two-sided t-test (n=110).

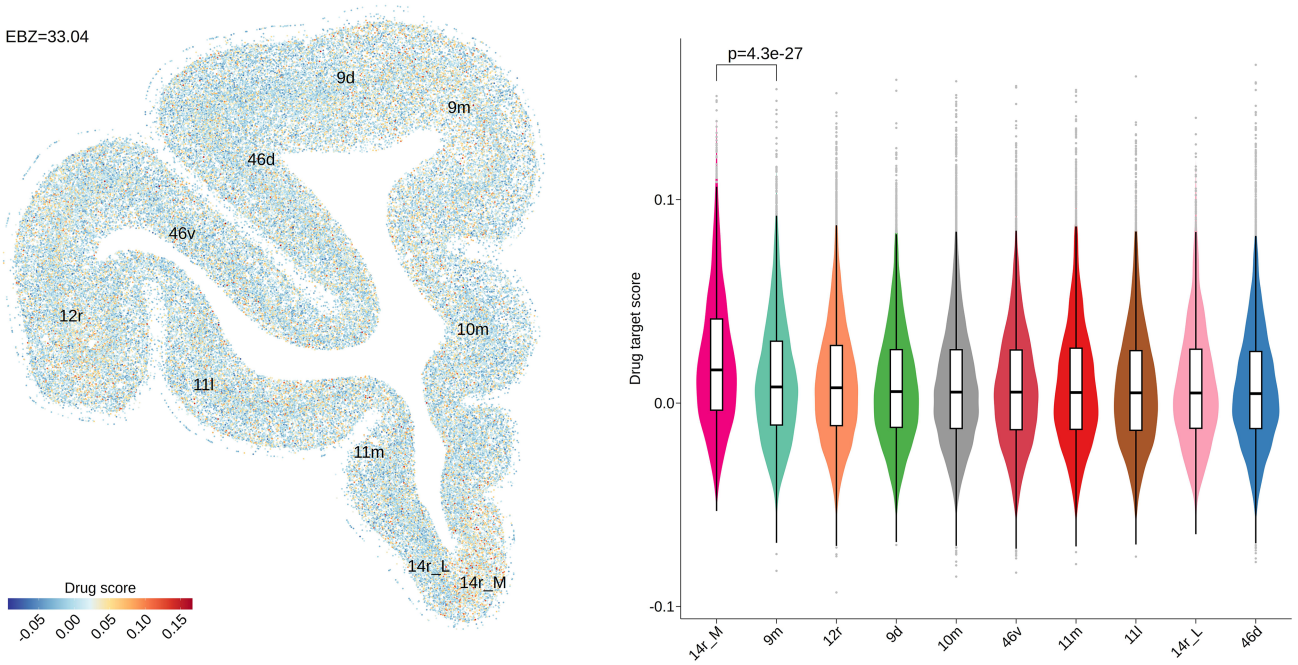

Extended Data Fig. 9 | Psychiatric drug module score. a) Drug module scores of individual cells in the macaque PFC ST data were calculated as the average expression level of 417 psychiatric drug target genes minus the average expression level of randomly selected control genes with matched expression characteristics, where each point represents a cell colored by its drug module score. b) Violin plot of drug module score in the medial side of PFC 14r, compared to that in each of the other regions. The black text shows the two-sided Wilcoxon rank sum test p-value ($n = 4,027$). In each box, the central line denotes the median, notches represent the 95% CI, the box indicates the IQR, and whiskers extend up to 1.5 times the IQR, with outliers shown as individual dots. 14r_L, 14r lateral side; 14r_M, 14r medial side.

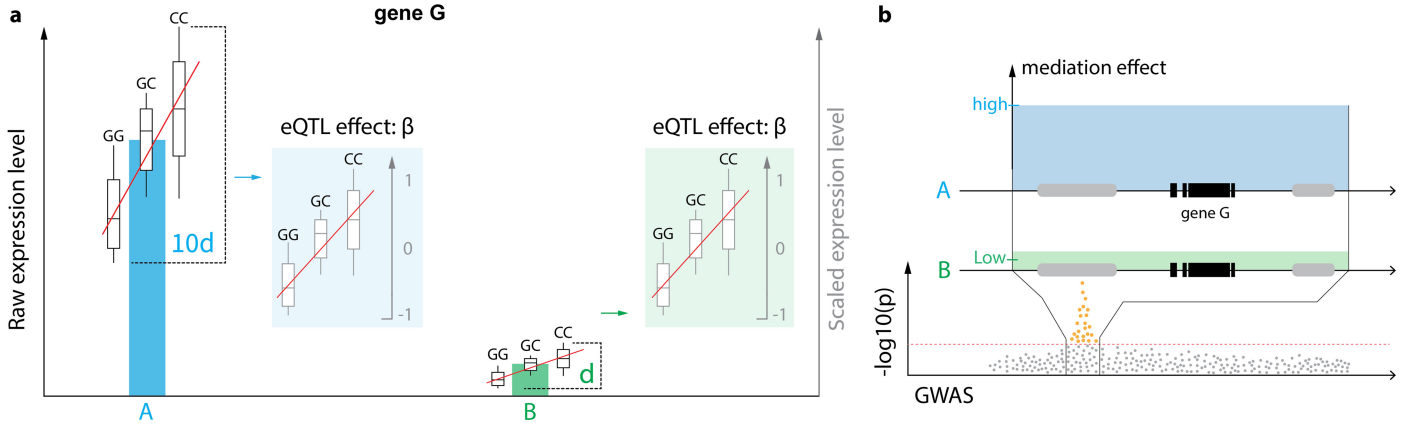

Extended Data Fig. 10 | Schematic representation of genetic effect mediated by eQTL effect in different cell groups with variable gene expression levels, in the absence of context-specific eQTL effects when expression levels are standardized within each context. a) There are mean and variance differences in expression of gene G between cell groups A and B. However, the eQTL effect size, which measures variations in gene expression levels amongst individuals carrying different genotypes, can remain consistent across these cell groups, irrespective of the differences in mean and variance of expression levels. b) Gene G exhibits higher expression levels in cell group A compared to group B. Even in the absence of context-dependent eQTL effects for the scaled expression levels, the impact of the eQTL variant on a complex trait, as mediated by different cell group, can differ due to variations in raw expression levels between cell groups. Note that a higher gene expression level often corresponds to a larger variance in gene expression due to the mean-variance relationship.

nature portfolio

Corresponding author(s): Jian Yang

Last updated by author(s): Jan 27, 2025

Reporting Summary

Nature Portfolio wishes to improve the reproducibility of the work that we publish. This form provides structure for consistency and transparency in reporting. For further information on Nature Portfolio policies, see our Editorial Policies and the Editorial Policy Checklist.

Statistics

For all statistical analyses, confirm that the following items are present in the figure legend, table legend, main text, or Methods section.

n/a	Confirmed	
☐	☒	The exact sample size (*n*) for each experimental group/condition, given as a discrete number and unit of measurement
☐	☒	A statement on whether measurements were taken from distinct samples or whether the same sample was measured repeatedly
☐	☒	The statistical test(s) used AND whether they are one- or two-sided *Only common tests should be described solely by name; describe more complex techniques in the Methods section.*
☐	☒	A description of all covariates tested
☐	☒	A description of any assumptions or corrections, such as tests of normality and adjustment for multiple comparisons
☐	☒	A full description of the statistical parameters including central tendency (e.g. means) or other basic estimates (e.g. regression coefficient) AND variation (e.g. standard deviation) or associated estimates of uncertainty (e.g. confidence intervals)
☐	☒	For null hypothesis testing, the test statistic (e.g. *F*, *t*, *r*) with confidence intervals, effect sizes, degrees of freedom and *P* value noted *Give P values as exact values whenever suitable.*
☒	☐	For Bayesian analysis, information on the choice of priors and Markov chain Monte Carlo settings
☒	☐	For hierarchical and complex designs, identification of the appropriate level for tests and full reporting of outcomes
☐	☒	Estimates of effect sizes (e.g. Cohen's *d*, Pearson's *r*), indicating how they were calculated

Our web collection on statistics for biologists contains articles on many of the points above.

Software and code

Policy information about availability of computer code

Data collection	No data-collection software was used.
Data analysis	We implemented our method in a Python package called gsMap. The source code is freely available at https://github.com/JianYang-Lab/gsMap. The other software or packages used in this study are summarized as follows: GCTA (v1.94.1): https://yanglab.westlake.edu.cn/software/gcta/#Overview plink (v1.90): https://www.cog-genomics.org/plink/2.0/ scanpy (v1.9.6): https://github.com/scverse/scanpy seurat (v4.4.0): https://github.com/satijalab/seurat scDRS (v1.03): https://github.com/martinjzhang/scDRS clusterProfiler (v3.18): https://github.com/YuLab-SMU/clusterProfiler LDSC (v1.01): https://github.com/bulik/ldsc biomaRt (v3.18): https://github.com/grimbough/biomaRt SMR (v1.3.1): https://yanglab.westlake.edu.cn/software/smr COLOC (v5.2.3): https://github.com/chr1swallace/coloc/ FUSION (v1.0.0): https://github.com/gusevlab/fusion_twas?tab=readme-ov-file PoPS (v0.2): https://github.com/FinucaneLab/pops

For manuscripts utilizing custom algorithms or software that are central to the research but not yet described in published literature, software must be made available to editors and reviewers. We strongly encourage code deposition in a community repository (e.g. GitHub). See the Nature Portfolio guidelines for submitting code & software for further information.

Data

Policy information about availability of data

All manuscripts must include a data availability statement. This statement should provide the following information, where applicable:

- Accession codes, unique identifiers, or web links for publicly available datasets
- A description of any restrictions on data availability
- For clinical datasets or third party data, please ensure that the statement adheres to our policy

We used GWAS summary statistics for 110 traits, as summarized in Supplementary Table 1.
The human embryonic ST data are available at https://ngdc.cncb.ac.cn/gsa-human/browse/HRA005567/.
The mouse embryonic and brain ST data are available at https://db.cngb.org/search/project/CNP0001543/.
The mouse brain MERFISH ST data are available at https://cellxgene.cziscience.com/collections/0cca8620-8dee-45d0-aef5-23f032a5cf09.
The macaque cortex ST data are available at https://db.cngb.org/search/project/CNP0002035/.
The ST data for human DLPFC are available at https://research.libd.org/globus/.
The scRNA-seq data from human and mouse are available at: https://cellxgene.cziscience.com/.
The reference LD data, generated from 1KGP3, are available at ftp://ftp.1000genomes.ebi.ac.uk/vol1/ftp/release/2013050.
The baseline annotations of LDSC are available at https://data.broadinstitute.org/alkesgroup/LDSCORE.
The DrugBank database is available at https://go.drugbank.com/releases/latest.
The Drug Repurposing Hub database (version of 3/24/2020) is available at https://repo-hub.broadinstitute.org/repurposing#download-data.
The human, mouse, and macaque reference genome data are available at https://nov2020.archive.ensembl.org/index.html.
The gsMap results for different traits and ST datasets can be visualized and downloaded at https://yanglab.westlake.edu.cn/gsmap/home.

Research involving human participants, their data, or biological material

Policy information about studies with human participants or human data. See also policy information about sex, gender (identity/presentation), and sexual orientation and race, ethnicity and racism.

Reporting on sex and gender	Sex and age were controlled for in the GWAS summary statistics in the original studies.
Reporting on race, ethnicity, or other socially relevant groupings	Participants were grouped into European, East Asian, Latino, and African American ancestral categories based on the reported information from the original GWAS studies. A detailed summary of the racial (ancestral) composition of each GWAS dataset is provided in Supplementary Table 1.
Population characteristics	Ancestries were controlled for in the GWAS summary statistics in the original studies.
Recruitment	We analyzed existing datasets. Thus, no recruitment was performed.
Ethics oversight	Ethics Committee of Westlake University (No. 20200722YJ001)

Note that full information on the approval of the study protocol must also be provided in the manuscript.

Field-specific reporting

Please select the one below that is the best fit for your research. If you are not sure, read the appropriate sections before making your selection.

☒ Life sciences ☐ Behavioural & social sciences ☐ Ecological, evolutionary & environmental sciences

For a reference copy of the document with all sections, see nature.com/documents/nr-reporting-summary-flat.pdf

Life sciences study design

All studies must disclose on these points even when the disclosure is negative.

Sample size	Spatial transcriptomics (ST) data: We included 54 coronal sections from 8 C57BL/6J mice (Mouse Embryonic ST Data), 62 transverse sections from a Carnegie Stage 8 (CS8) human embryo of Chinese ancestry (Human Embryonic ST Data), 2 sections from an adult C57BL/6J mouse brain and an E16.5 embryonic C57BL/6J mouse brain (Mouse Brain ST Data), 2 sections from an adult C57BL/6J-1 mouse brain (Mouse Brain MERFISH ST Data), 162 coronal sections from 3 adult cynomolgus monkeys (Macaque Cortical ST Data), and 8 coronal sections from 2 adult donors of European ancestry (Human DLPFC ST Data). Human GWAS data: Summary statistics from 110 complex traits GWAS were analyzed, with an average sample size of 385,000 individuals. Detailed sample sizes for each GWAS are provided in Supplementary Table 1.
Data exclusions	For the human dorsolateral prefrontal cortex (DLPFC) spatial transcriptomics (ST) data, we excluded the ST sections from individual #3 (sections 151669, 151670, 151671, and 151672) because these four sections lacked spots corresponding to cortical layers 1 and 2. All other data from the original dataset were included and utilized in this study.
Replication	We replicated our results using independent biological samples from different datasets. Mouse Embryonic ST Data: We replicated results across 54 sections from 8 mice.

Human Embryonic ST Data: We replicated results across 68 sections from 1 human donor.
Mouse Brain ST Data: We replicated results across 4 sections from 4 mice.
Macaque Cortical ST Data: We replicated results across 162 sections from 3 monkeys.
Human DLPFC ST Data: We replicated results across 8 sections from 2 human donors.
All replication analyses were successful.

Randomization

We conducted analyses using existing datasets, thus no randomization was applied to data generation. Covariates such as sex, age, and ancestry PCs were controlled for in the GWAS summary statistics from the original studies.

Blinding

We conducted analyses on existing datasets, and therefore, no blinding measures were implemented during this study.

Reporting for specific materials, systems and methods

We require information from authors about some types of materials, experimental systems and methods used in many studies. Here, indicate whether each material, system or method listed is relevant to your study. If you are not sure if a list item applies to your research, read the appropriate section before selecting a response.

Materials & experimental systems

n/a	Involved in the study
☒	☐ Antibodies
☒	☐ Eukaryotic cell lines
☒	☐ Palaeontology and archaeology
☒	☐ Animals and other organisms
☒	☐ Clinical data
☒	☐ Dual use research of concern
☒	☐ Plants

Methods

n/a	Involved in the study
☒	☐ ChIP-seq
☒	☐ Flow cytometry
☒	☐ MRI-based neuroimaging

Plants

Seed stocks

NA

Novel plant genotypes

NA

Authentication

NA